Master's thesis

NTNU
Norwegian University of Science and Technology
Faculty of Engineering
Department of Energy and Process Engineering

Simon Margido Urdahl

Influencing fish migration by creating and altering vortices in turbulent flow

Master's thesis in Energy and Environmental Engineering
Supervisor: Ole Gunnar Dahlhaug
Co-supervisor: Bjørn Winther Solemslie and Kristian F. Sagmo
June 2022

NTNU
Norwegian University of Science and Technology

Simon Margido Urdahl

Influencing fish migration by creating and altering vortices in turbulent flow

Master's thesis in Energy and Environmental Engineering
Supervisor: Ole Gunnar Dahlhaug
Co-supervisor: Bjørn Winther Solemslie and Kristian F. Sagmo
June 2022

Norwegian University of Science and Technology
Faculty of Engineering
Department of Energy and Process Engineering

NTNU
Norwegian University of
Science and Technology

Preface

This thesis is written at the Hydropower Laboratory at the Norwegian University of Science and Technology for the FishPath project. The initial intent was to do measurements in the biggest water channel facility at the laboratory, and preparations for this were made. Due to continuous delays in experimental equipment delivery, the measurements were moved to a smaller facility in late April. This meant adjusting the goals of the results based on what was possible in the new type of facility. Three weeks of lab work resulted in measurements 27.05.2022. The reader should therefore be aware that there was sparse time between acquiring the data sets from the measurements and the delivery 15.06.2022.

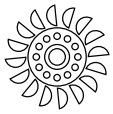

Waterpower Laboratory

NTNU

Abstract

Fish entering hydropower intakes today is too high, and fish mortality should be reduced. The FishPath project seeks to guide fish migrating downstream rivers away from intakes by turbulent flow. To enable this, more knowledge is needed about how specific hydrodynamic properties relate to migrating fish. This thesis aims to create and describe different types of hydrodynamic properties in turbulent flow. A literature review has been carried out on how specific turbulent flow is triggered by three different shapes exposed to water flow, namely a short cylinder with a D-shaped cross section (D-cylinder), a short cylinder with a triangular cross section (spear) and a delta ramp vortex generator. An experimental campaign using particle image velocimetry (PIV), to study the flow behind the spear has also been conducted. This experiment serves as a start-up for more measurements to come, as well as a basis for comparison with computational fluid dynamics (CFD) simulations by SINTEF of the same type of flows.

The literature review concludes that the spear will most likely create a slightly wider wake with more circulation than the D-cylinder. They have a height to diameter ratio of between one and two, and the three dimensional effects will dominate, making it very difficult to predict the flow due to its complexity and Reynolds number-dependency. The delta ramp will create streamwise vortices, but will likely lose its vorticity fast, so a filled delta wing vortex generator is suggested as an alternative. The PIV measurements of the spear shows the transition between the recirculation zone and the wake further downstream. The recirculation zone is dominated by two symmetrical circulating areas with substantial backflow separated by a small region of downstream flow. The streamwise velocity profiles flatten drastically after the recirculation zone. This flow deviates from a idealistic two dimensional flow, which indicates a strong effect from the three-dimensional flow induced

at the top of the spear which influences the flow at the measurement plane. The simulations show a similar recirculating structure, but the transition from the recirculation area is less drastic, and the streamwise velocity profiles deviate highly from the PIV at the downstream part of the field of view. The result will likely be highly sensitive to the vertical placement of the measurement planes due to considerable three-dimensional effects in this area, and a small deviation of the placement between the simulations and the experiment could be the reason.

Vannkraftlaboratoriet

NTNU

Sammendrag

Idag er det for mye fisk som havner i inntakene på vannkraftverk, og fiskedødeligheten bør reduseres. FishPath-prosjektet ønsker å veilede fisk som migrer nedstrøms ved hjelp av turbulent strømning. For å få til det, må forståelsen for hvordan fisker reagerer på spesifikke hydrodynamiske egenskaper økes. Denne tesen har prøvd å skape, samt beskrive spesifikke hydrodynamiske egenskaper i turbulente strømninger. Det har blitt gjort et literaturstudie på spesifikk turbulent strømning som skapes av tre forskjellige former utsatt for vann. Disse er en kort sylinder med D-formed tverrsnitt (D-sylinder), en kort sylinder med et trekantet tverrsnitt (spyd), samt en deltarampe virvelgenerator. Det har også blitt utført et eksperiment av typen partikkel bilde velosimetri (PIV), for å undersøke strømningen bak spydet. Dette eksperimentet skal fungere som oppstarten for flere av disse type målinger, men også for å sammenligne vaken bak spydet med numerisk fluiddynamikk-simuleringer (CFD) gjort på samme type strømning utført av SINTEF.

Literaturstudiet konkluderer med at spydet will mest sannsynlig lage en litt bredere vake og ha større sirkulasjon enn D-sylinderen. De har en høyde over diameter ratio på mellom en og to, som indikerer sterke tredimensjonale effekter, noe som vil gjøre det svært vanskelig å anslå hvordan strømningen vil bli seende ut. Deltarampen vil kunne lage strømvise virvler, men vil raskt miste sirkuleringen, derfor er en deltavinge som er fylt med masse under foreslått som et alternativ. Målingene av spydet viser overgangen mellom resirkuleringssonen og vaken lenger nedstrøms. Resirkuleringssonen er påvirket av to symmetriske sirkulerende arealer med tydelig bakoverstrømning som er separert av et lite område med strømning nedstrøms. De strømvise hastighetsprofilene flater ut drastisk etter resirkuleringssonen. Dette avviker fra en idealisert to-dimensjonal strømning, noe som indikerer en sterk påvrikning av tre dimensjonale effekter indusert på toppen av spy-

det. Simuleringene viser en lignende resirkuleringsstruktur, men overgangen mellom denne sonen og vaken lengre nedstrøms er mindre drastisk, og de strømvise hastighetsprofilene avviker kraftig fra PIV-målingene i nedstrøms del av domenet. Resultatet vil sannsynligvis være sensitiv til den vertikale plasseringen av målingsplanet grunnet betraktelige tre-dimensjonale effekter i dette området, slik at et lite avvik i plasseringen mellom simuleringen og målingene kan være grunnen til at resultatene er forskjellig.

Acknowledgments

Several people have contributed to this thesis. This thesis was written at the Hydropower Laboratory at the Norwegian University of Technology and Science, and first and foremost, I want to thank the community at the laboratory, both students and academic staff, for a fun and academically rewarding year. I would like to thank my supervisor Ole Gunnar Dahlhaug, for making this thesis possible by including me in the FishPath project, and facilitating the process from start-up to completion. Furthermore, I would like to thank my co-supervisors, Bjørn Winther Solemslie and Kristian F. Sagmo. Bjørn has assisted me throughout this thesis with valuable technical insights, helping me with my literature review as well as the experimental set-up. Kristian has contributed with his knowledge of particle image velocimetry experiments, and together with PhD-candidate Gabriele Gaiti, we have spent long days at the lab to be able to complete my experiments in time. This is greatly appreciated. I would also like to thank Marcell Szabo-Meszaros for giving me access to his computational fluid dynamic simulations and being helpful when I had questions about them. Lastly, I would like to thank Gütle Vera Franziska and Albayrak Ismail for hosting my visit to ETH in Zürich, where I was able to facilitate the start-up of experiments on fish, which will later be used together with results from the Waterpower Laboratory.

Contents

List of tables

List of figures

Nomenclature

Abbreviation

2-D	Two-dimensional
3-D	Three-dimensional
BL	Boundary layer (m)
CCD	Charge-Coupled Device
CFD	Computational fluid dynamic
CMOS	Complementary metal-oxide-semiconductor
ETH	Swiss Federal Institute of Technology
FFT	Fast Fourier Transform
FOV	Field Of View
IA	Interrogation Area
NINA	Norwegian Institute for Nature Research
NTNU	Norwegian University of Science and Technology
PIV	Particle Image Velocimetry
TKE	Turbulent Kinetic Energy (W)
VKL	Waterpower Laboratory

Latin symbols

A	Area (m^2)
C_s	Scattering cross section (m^2)
$\mathbf{D}_1$	Two dimensional displacement vector in the image plane (m)
D	Diameter of vortex generators (m)
D_1	Displacement length in the image plane (m)
d_p	Diameter of tracer particle (m)
D_z	Displacement length in the vertical direction in the image plane (m)
d_{cell}	Cell size of honeycomb (m)
d_{ppd}	Particle image diameter (Pixels)
I	Image intensity field of the first exposure (Wm^{-2})
I'	Image intensity field of the second exposure (Wm^{-2})
I_0	Laser intensity (Wm^{-2})
l	Wake half width in the transverse direction (m)
L_e	Length scale of an eddy (m)
L_f	Length scale of a fish (m)
l_x	Length of a interrogation window in the streamwise direction (m)
l_y	Length of a interrogation window in the transverse direction (m)
l_z	Length of the light sheet thickness (m)
N_{ppp}	Particles per pixel (ppp)
P_s	Total scattered power (W)
R_D	Correlation plane for $\mathbf{s} \approx \mathbf{D}_1$ (W^2m^{-4})
$R_F \& R_C$	Results of the correlation plane where $\mathbf{s} \neq \mathbf{D}_1$ (W^2m^{-4})
$\mathbf{s}$	Separation vector (m)
S	Surface area (m^2)
s	Side length of honeycomb cell (m)

t	Time (s)
U	Mean velocity in the streamwise direction of a time series (ms^{-1})
u	Velocity in streamwise direction (ms^{-1})
u'	Fluctuation velocity in streamwise direction (ms^{-1})
U_∞	Free stream velocity in the streamwise direction (ms^{-1})
U_s	Velocity deficit in the streamwise direction (ms^{-1})
w'	Fluctuation velocity in the vertical direction (ms^{-1})
$\mathbf{V}$	Three dimensional velocity vector (ms^{-1})
v	Velocity in the transverse direction (ms^{-1})
v'	Fluctuation velocity in the transverse direction (ms^{-1})
w	Velocity in vertical direction (ms^{-1})
X	Arbitrary quantity
x	Streamwise direction (m)
y	Transverse direction (m)
z	Vertical direction (m)

Dimensionless numbers

AR	Aspect ratio
F_0	Out-of-plane loss factor
F_1	In-plane loss factor
k	Auto-correlation constant
M	Magnification factor
N	Effective particle image
n	Refractive index
N_1	Number of particles in an interrogation window
q	Normalized particle diameter

r	Structure to flow ratio
Re	Reynolds number
SNR	Signal to noise ratio
St	Strouhal number

Greek symbols

β	Porosity $(-)$
δ	Total error
ϵ	Systematic error
Γ	Circulation $(m^2 s^{-1})$
λ	Light wave length (m)
μ	Dynamic viscosity $(Pa\ s)$
ν	Kinematic viscosity $(m^2 s^{-1})$
Ψ	Delta ramp angle $(-)$
ρ	Mass density (kgm^{-3})
σ	Standard deviation
σ_A	Noise free image (Wm^{-2})
σ_n	Noise in image (Wm^{-2})
τ_p	Response time (s)
θ	Yaw angle (deg)
ζ	Vorticity vector (s^{-1})

Chapter 1

Introduction

This chapter will cover the background of why this thesis is relevant, and then explain the objective and scope. The master thesis agreement can be seen in Appendix A.

1.1 Background

The sixth report on climate change, published by the U.N. in 2022, [12] depicts a staggering truth: if humanity does not act now, the planet will suffer irreversible damage that can threaten a livable future. The emissions of greenhouse gases (GHG) must be substantially decreased, but access to energy is important for the prosperity of humanity. Because renewable energy emits far less greenhouse gases than fossil fuels, it can be a part of the solution.

Hydropower is a renewable energy source with the added benefit of flexibility. The water can run through the turbines on high demanding days or be stored in dams when the other less flexible energy sources such as wind turbines and solar panels produce a high amount of energy. Furthermore, hydropower has a high power efficiency and low running costs compared to other energy sources, and up to 70% of the economically feasible potential in the world is yet to be built, especially in developing countries where energy is highly needed [13].

Despite all the benefits of hydropower, there is still a need for major interference in nature. Big hydro power dams can among other things change the water quality, the flow of rivers and harm the biodiversity of the ecological system [14]. One problem is fish entering the powerplant intakes. Today, the fish mortality is too high and should be reduced. There exists solutions to

this, like building fine meshed racks or other structures, but this is often expensive and requires big constructions in the river.

1.2 Objective and scope

FishPath is a research project that aims to guide fish migrating downstream away from hydropower intakes with turbulent flow. The project is led by the Norwegian Institute for Nature Research (NINA), which is in charge of the biological aspects of the project. The Swiss Federal Institute of Technology (ETH) in Zurich will do experiments on fish in a water flume. This thesis is written for the Waterpower Laboratory (VKL) at the Norwegian University of Science and Technology (NTNU), which has the responsibility for studying the flow. This is important because FishPath needs to relate flow properties to how the fish react. Understanding these relations can help hydropower plants guide the fish in the correct direction. SINTEF will provide the project with computational fluid dynamics (CFD) simulations, but this needs to be verified by experiments done by VKL.

Experiments on creating and analyzing certain turbulent flows will be held in a water channel at VKL, which will correspond to the flow that the fish at ETH will experience. The experiments will be done using Particle Image Velocimetry (PIV), which is an optical experimental method for obtaining velocity fields of water flow. This thesis will prepare for this experiment, but the experimental rig will not be ready until after this thesis is written. Therefore, PIV experiments will be conducted in a smaller duct at VKL for this thesis. Here, it is not possible to get a full perspective of the flow, but the small field of view can be used to study a specific part of the wake, as well as compare this area to the CFD simulations. A literature review on the specific shapes that will be placed in the flow to trigger specific turbulent flows will be done to get a broader understanding.

The result of FishPath will likely consist of multiple structures in the river, each consisting of several shapes that trigger turbulent movements. For this thesis, only single shapes on a hydrofoil will be investigated. The reason for applying single shapes is because it is the start of the FishPath project, which will last to 2026. Simple PIV measurements are a good start, and will also serve to validate the novel simulations by SINTEF. If these simulations are validated, the project can continue with more complex flows and ultimately decide which set of shapes that make the best influence on fish migrating downstream.

Chapter 2

Theory

To be able to explain literature, the experiment and the results, some theory regarding fluid flow and particle image velocimetry (PIV) is needed.

2.1 Fluid flow

This section will cover theory regarding fluid flow and will focus on vortices, turbulence and wakes.

2.1.1 Vortex

A vortex is, according to Cengel and Cimbala, a local structure in a fluid characterized by a concentration of vorticity, i.e. a fluid particle that spins or rotates. The vorticity is a measure of how much the fluid particle spins or rotates and can be calculated using Equation 2.1.

$$\zeta = \nabla \times \mathbf{V} = curl(\mathbf{V}) \tag{2.1}$$

ζ is the vorticity and $\mathbf{V}$ is the velocity vector [15]. Another measure relating to a vortical flow (a flow with significant levels of vorticity) is the circulation. This can be characterized as the strength of the vortex and can be calculated using Equation 2.2 [16].

$$\Gamma = -\iint_{dS} (\nabla \times \mathbf{V})\, dS \tag{2.2}$$

where S is the surface area.

2.1.2 Turbulence

There is no universal definition of turbulence, but it can be characterized as chaotic flow. Cengel and Cimbala define turbulent flow as "an unstable, disordered state of vortical fluid flow that is inherently unsteady and that contains eddying motions over a wide range of sizes (or scales)" [15]. Eddying motion can be described as vortices with velocity. The Reynolds number is the ratio between momentum and viscosity as seen in Equation 2.3, and if this gets sufficiently large, the flow will be turbulent. This is because the large eddying motions will not be damped by viscosity. Instead, they will break into smaller sizes, thus creating a flow with a wide range of scales as mentioned in the definition of turbulence above. The smallest scales of motion will be dissipated into heat. Pope [17] divides the sizes of eddies in an energy containing length scale (these eddies contains the bulk of the energy of the flow), the inertial range (small eddies where motion is determined by inertial effects) and the dissipation range (small eddies where viscous effects are dominant).

$$Re_x = \frac{uL_c}{\nu} \tag{2.3}$$

In the equation above, ν is the kinematic viscosity, L_c is the characteristic length of an object and u is the velocity component in the streamwise (x) direction. Each velocity component in a time series, i.e. u, can be divided into a mean velocity (U) and a fluctuating velocity (u') as seen in Equation 2.4 [17].

$$u = U + u' \tag{2.4}$$

One way to measure the amount of turbulence is to look at the turbulent kinetic energy (TKE). This is the mean kinetic energy per unit mass in a fluctuating velocity field, and can be calculated using Equation 2.5, where v and w are the velocity components in the transverse (y) and vertical (z) directions respectively.

$$TKE = \frac{1}{2}\langle \mathbf{V}' \cdot \mathbf{V}' \rangle = \frac{1}{2}(\overline{u'^2} + \overline{v'^2} + \overline{w'^2}) \tag{2.5}$$

A velocity measurement of turbulent flow can be difficult because there exists many different scales of velocity fluctuations. One way to analyze the flow is to do a Fourier analysis, where the velocity time signals are converted

into several sine functions of varying frequencies [17]. The velocity time signals are therefore converted into a frequency based signal. If one specific frequency occurs frequently, this can mean that a vortex shedding (see next subsection) of that frequency may be present at this location.

2.1.3 Wake

"A wake is a region behind a body which is dominated by frictional force, viscous stress and vorticity, often accompanied by turbulence" is how Cengel and Cimbala define a wake [15]. It is formed by boundary layers that are separated from the surface of a body on each side. The separated boundary layers create a shear layer with the free stream velocity (U_∞) on each side of the body. The shear layers are the catalyst for vortical flow in the wake region. To describe the velocity in the wake, the velocity deficit (U_s) is often used, and can be calculated using Equation 2.6 [17]. l denotes the half width of the wake. U_s and l are illustrated in Figure 2.1 and are dependent on the position in the streamwise and transverse direction.

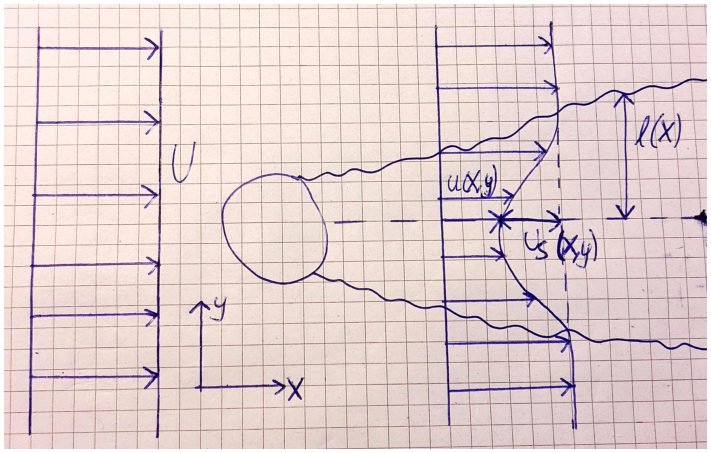

Figure 2.1: Illustration of the main components of a wake. U_s is the velocity deficit in the wake, U is the free stream velocity and l is the wake half width. This is a modified illustration of a picture that is also used in the project thesis of the author [1].

$$U_s = U_\infty - u(y) \tag{2.6}$$

Inside a wake, a phenomenon called vortex shedding can occur. Vortex

shedding is when the vortices formed in the wake are moved downstream by the bulk velocity. The vortices formed from each side of the body can alternate downstream and create a flow pattern of altering vortices. This phenomenon is called Von Karman shedding [6], and can be seen in Figure 2.2.

Figure 2.2: Von karman shedding [2]

There exists a non-dimensional number called the Strouhal number (St) which relates the characteristic length of the object, the frequency of the shedding (f) and the freestream velocity, as seen in Equation 2.7 [15]. The Strouhal number of various shapes have been found empirically and can therefore be used to find the frequency of the shedding.

$$St = \frac{fL_c}{U_\infty} \tag{2.7}$$

2.2 Particle image velocimetry theory

Particle Image Velocimetry (PIV) is an experimental method to determine the velocity field of a flow. It accesses the flow optically, which means that PIV is a non intrusive method; no probes or other measurement devices need to be put into the flow, which is one of the main advantages of PIV. Essentially, PIV is determining the velocity field by determining how far tracer particles in the flow have shifted, ($\mathbf{D}_1$), in a certain time, Δt. The tracer particles in the field of interest (FOV) are illuminated by a laser in two subse-

quent pulses, and a camera captures images perpendicular to the scattered light of the particles. Using only one camera, a two-dimensional velocity field is achieved. All three velocity components for the specific measurement plane can be achieved using two cameras. This is called stereoscopic PIV. The FOV is divided into small cells called interrogation areas (IA), and a mathematical approach using statistics determines how far the tracer particles have moved for each IA. A conceptual figure showing the concept of PIV can be seen in Figure 2.3. To get good PIV measurements, a deeper knowledge of the different aspects of PIV is needed, and this will therefore follow in this subsection [3].

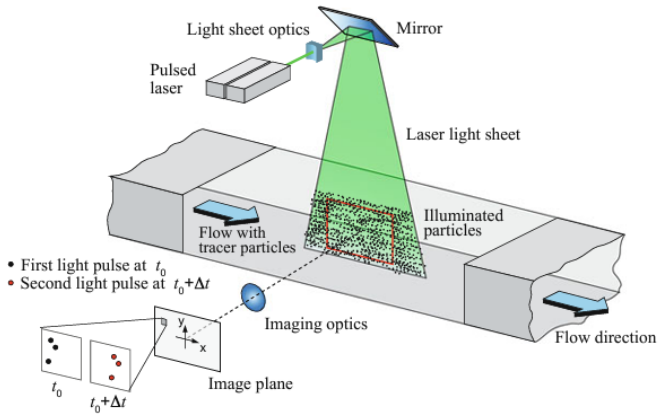

Figure 2.3: The concept of particle image velocimetry [3]

2.2.1 Tracer particles

Tracer particles are added to the flow and they should follow the flow. Therefore, the density of the particles must be close to the density of the fluid, so that they are naturally buoyant. If there is a considerable difference, the particles will either rise or sink due to gravitational and buoyant forces, and the particles will have a lag compared to the fluid. The lagging time is known as response time (τ_p), and it can be calculated using Equation 2.8 if the particles are nearly naturally buoyant and Stokes' flow is assumed. Stokes flow is valid for Re $<<$ 1 [15]. Equation 2.8 implies that the response time is proportional to the square of particle diameter (d_p) and the difference in density (ρ), while inversely proportional to the dynamic viscosity (μ). In

most PIV applications, the Reynolds number of the particles will exceed 1, but Equation 2.8 can still be used to get an indication of which variables affect the response time.

$$\tau_p = \frac{d_p^2 \Delta\rho}{18\mu}. \tag{2.8}$$

A good PIV measurement requires homogeneously distributed tracer particles. For liquids, this is easier to achieve than for gases, and can in most cases be added and mixed prior to the FOV. Centrifugal forces can create dishomogeneity, and one specific case of this is vortices. Here, particles can be pushed outside of the vortex core.

The tracer particles should scatter the light from the laser in such a way that it is easy to photograph. This is because the image intensity is directly proportional to the light scattering. Light scattering can easily be increased by increasing the laser power or choosing particles that have good light scattering properties. The last option is often the most economical. Important parameters for light scattering are size, orientation, shape and the refractive index ratio between the fluid and the particle. More on scattering behaviour in the next subsection.

2.2.2 Illumination

For the camera to be able to record the tracer particles, the FOV must be illuminated. The choice for most PIV applications is using a laser. This is because a laser can emit monochromatic light (light with only one wavelength), have high energy density, the ability to make thin light sheets and the ability to create pulses of light with short time intervals.

As mentioned in subsection 2.2.1, the scattering of the tracing particles depends not only on the laser properties, but also on particle and fluid properties. An important fluid parameter is the refractive index (n), and if it is low, there is more powerful scattering. Because water has a 10 times bigger refractive index that of air, larger particles need to account for the low scattering in water. One way to quantify the amount of light scattering is to investigate the scattering cross section (C_s), which can be calculated using Equation 2.9

$$C_s = \frac{P_s}{I_0}, \tag{2.9}$$

where P_s is total scattered power and I_0 is laser intensity. C_s can be seen as a function of the particle diameter over wavelength (λ) in Figure 2.5. What this figure clearly shows, is that a diameter bigger than the wavelength of the laser should be assured. This region is called Mie scattering, while the region for smaller diameters is called Rayleigh scattering. One important parameter in the Mie scattering regime is the normalized diameter (q) as seen in Equation 2.10. This parameter can be used to foresee how the light spreads. If q is small, the light is mostly scattered behind the particle, while increasing q will scatter the light in front of the particle too, which is wanted for PIV measurements. This is illustrated in Figure 2.4.

$$q = \frac{\pi d_p}{\lambda} \tag{2.10}$$

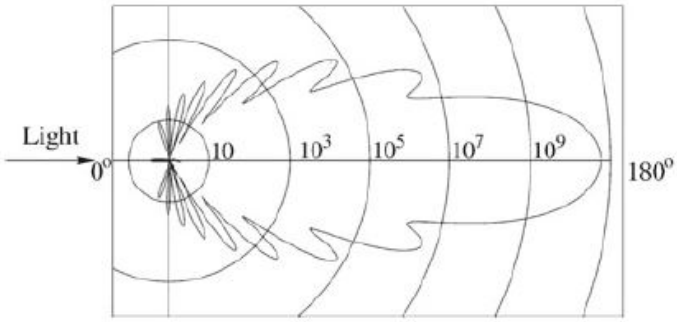

(a) Oil particle, 1μm

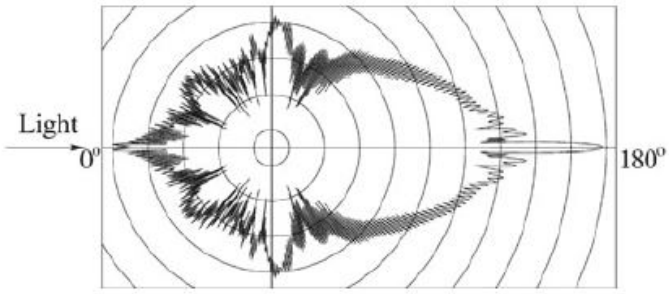

(b) Oil particle, 10μm

Figure 2.4: Light scattering of two differently sized oil particles [3].

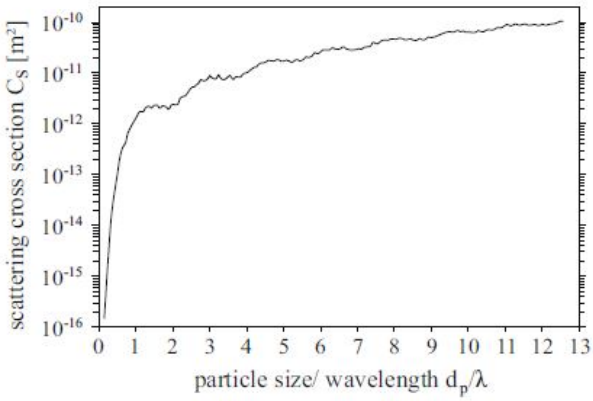

Figure 2.5: Scattering cross section as a function of particle diameter over wavelength [3]

2.2.3 Recording and calibration

The light that is reflected by the tracer particles needs to be captured by a camera. The PIV recording usually requires at least 0.05–0.1 seconds between each picture, and the bottleneck is the data transferred from the sensor in the camera to memory. Preferably, one single frame for each illumination should be performed. If only one frame for both illuminations is possible, it is hard to know which direction the particles went. A calibration needs to be done before the real measurements can be made. This means finding a relation between the displacement on recordings and the real displacement, see Equation 2.11.

$$[u, v] = \frac{1}{M} \frac{\mathbf{D}_1}{\Delta t} \tag{2.11}$$

M in the above equation is the magnification factor. Other parameters that must be evaluated are the size of particle images, size of interrogation areas, number of particle images within interrogation areas and number of interrogation areas. This needs to be optimized while monitoring, and the reason for this is to reduce the systematic error of the measurements. More on that in subsection 2.2.5.

PIV can be recorded with high spatial resolution. The interrogation areas need to be small enough so that big velocity gradients will not affect

the results outside their influence. The sensor of the camera decides the number of independent velocity vectors possible. The bandwidth of scales that can be resolved (data per second) depends on spatial resolution and the FOV size. This can be solved with better sensors or two cameras.

Often, there are lower repetition rates, i.e. lower temporal resolution. This is because data from the two frames must be transferred, which can be time-consuming. The two main choices for a camera sensor in PIV today are the Charge-Coupled Device (CCD) and the Complementary metal-oxide-semiconductor (CMOS). Historically, the CCD has been the number one choice, but CMOS has increased its popularity lately for fast readout rates and therefore increasing the temporal resolution.

2.2.4 Evaluation

After taking two subsequent pictures with a time delay, the distance travelled in that time must be calculated. Here, cross correlation is a useful technique which find the most likely distance travelled by identifying the displacement vector ($\mathbf{D}_1$) that relates the two pictures the best. One way to do so is to multiply the light intensities from the first picture (I) with the intensities of the second picture (I'). The result is the correlation plane ($R_{||}$), see Equation 2.12.

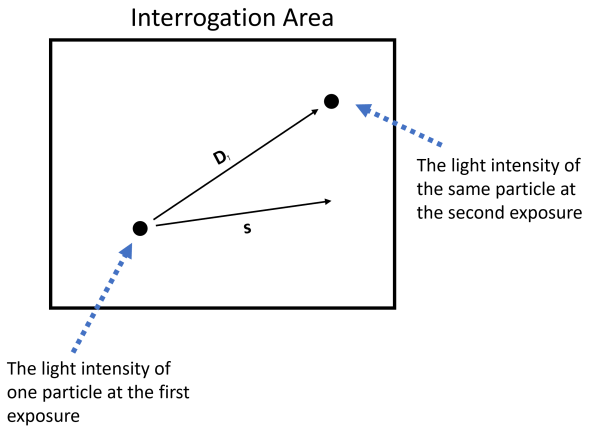

Figure 2.6: The light intensities of one particles in the first and second exposure of a PIV measurement. **D** is the real displacement, while the separation vector **s** is a guess of the displacement.

$$R_{||}(\mathbf{s}) = I([M \cdot x, M \cdot y]) \cdot I'([M \cdot x, M \cdot y] + \mathbf{s}), \tag{2.12}$$

where **s** is the separation vector between the intensities of the two pictures. The separation variable and the displacement are illustrated in Figure 2.6.

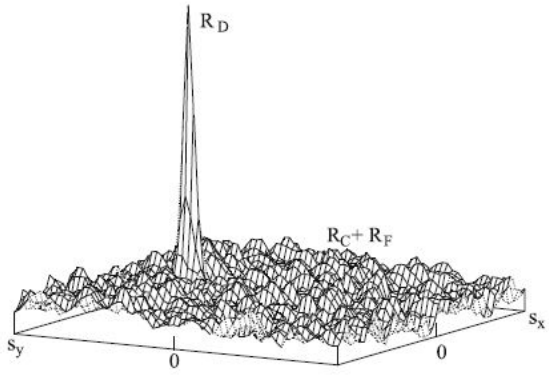

Figure 2.7: The correlation plane of the intensities of two single exposed frames. R_C and R_F represent noise, while R_D represent the correlation plane when the separation variable ($\mathbf{s} = [S_x, S_y]$) is roughly equal to the real displacement [3].

When the separation variable is close to the real displacement, the R_D correlation function appears, and if not, different types of noise are achieved (R_C and R_F), see Figure 2.7. This means that locating the maximum of R_D, will locate the displacement of the tracer particles after Δt.

Equation 2.12 is computationally expensive to calculate numerically, so it is common to use the Fast Fourier Transform (FFT) algorithm. It takes the Fourier transform of the camera intensities, multiplies them and transform the result back to real values. This is a recognized method for calculating the correlation plane in a computationally cheaper way.

The correlation for each set of pictures can be done in one step, or in a more iterative approach. One iterative approach that can increase the accuracy, but also increase the computation time, is multi pass. Here, a standard correlation procedure is performed, then more calculations are performed where the interrogation windows get an offset close to the displacement of the previous correlation. A further improvement to this is grid refining schemes, where the interrogation windows start with a large size, and then are decreased when more information about the displacements is uncovered.

A problem that can occur with flows with vortices is that a linear representation of the velocity can be insufficient and can result in multiple peaks in the correlation plane. One way around this is to deform the image. This is a multi-pass method where the interrogation windows are deformed based on earlier displacement estimates. This is illustrated in Figure 2.8. This deformation can estimate flows with vortices better.

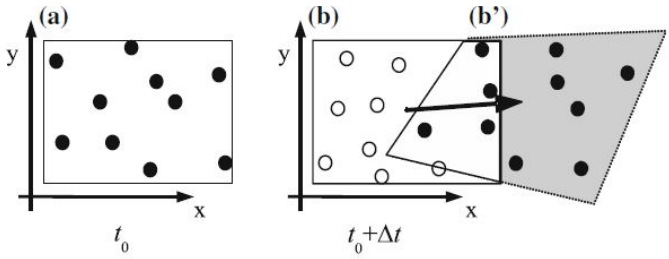

Figure 2.8: Deformation of interrogation window from the time t_0 to $t_0 + \Delta t$ [3]

After the data has been cross-correlated, the results must be evaluated. There are several methods to improve the results. One way is to apply different filters to the image. Intensities that exceed or subceed a certain threshold can be removed. This is called intensity capping. Another method is to provide a filter that does the same as intensity capping, but the criteria change throughout the picture. This is called the min/max filter, and was suggested by Westerweel [18]. After all measures to create valid PIV measurements with low error have been performed, there will still be wrong velocity vectors in the velocity dataset that do not belong to the velocity field. Westerweel named these "spurious vectors," and some of them are inevitable. There are many algorithms that can remove these vectors, and both commercial and open source PIV software will usually have solutions for this.

2.2.5 Error and uncertainty

Every experiment will have measurements that contain an error. A measurement ($X_{measured}$) can be divided into a real value (X_{true}) and an error (δ_x), see Equation 2.13.

$$X_{measured} = X_{true} + \delta_X \tag{2.13}$$

The error can further be divided into a systematic error and a random error. A systematic error (ϵ) is often constant and can be errors related to the calibration or instruments that does not perfectly captures the reality. The random error (σ) is described as a standard deviation, see Equation 2.14. The relation between systematic and random errors is depicted in Figure 2.9.

$$\sigma_X = \sqrt{\frac{1}{N-1}\sum_{i=1}^{n}(X_i - \langle X \rangle)^2} \tag{2.14}$$

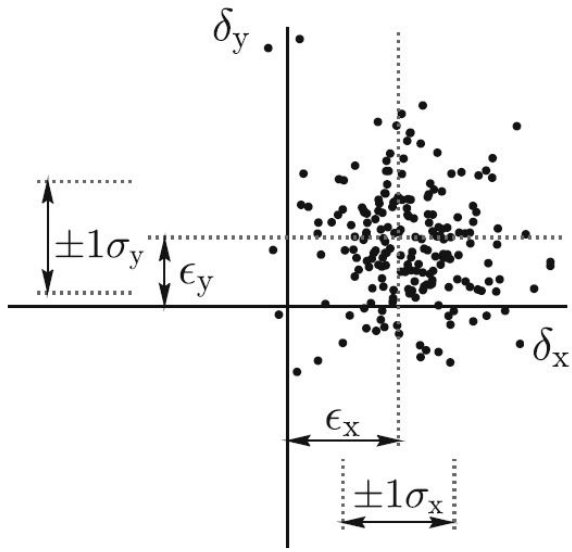

Figure 2.9: The relation between the systematic error (ϵ) and the random error (σ). δ denotes the total error. [3]

It is difficult to quantify how big the error is, and the term "uncertainty" is related to this. It is desirable to quantify an interval where the real value is present. If the uncertainty is reduced, the interval is shortened. One goal of a good PIV experiment is to reduce the uncertainty as much as possible. The PIV software, DaVis 8.4, quantifies the random error by Equation 2.15 [19].

$$\Delta V = \frac{\sigma_V}{k} \tag{2.15}$$

k is the number of images in the measurement set if all the samples of

V are completely independent. This is not the case for all images, because the measurements of V will have some correlation with its previous and next images. k is computed using the auto-correlation of the velocity time-series. The following common reasons for systematic error will be introduced:

- Number of effective particle images
- Dynamic Velocity Range (DVR)
- Dynamic Spatial Range (DVR)
- Diameter of particles
- Peak locking
- Background noise
- Curvature of streamlines

Effective particle images

One source of error is having too few effective particle images (N) in an interrogation window. N is a product of three factors, which include the effect of particles disappearing from the window after the time interval. N can be calculated using Equation 2.16.

$$N = N_1 F_0 F_1 \tag{2.16}$$

where N_1 is the number of particles in one IA at the first exposure, F_0 is the factor describing out-of-plane loss of pairs and F_1 is the factor describing in-plane loss of particle pairs. F_0 and F_1 can be calculated using Equation 2.17 and Equation 2.18.

$$F_0 = (1 - \frac{l_z}{D_z}) \tag{2.17}$$

$$F_1 = (1 - \frac{l_x}{D_1})(1 - \frac{l_y}{D_1}) \tag{2.18}$$

D_z is the displacement out of the plane, l_x and l_y are the sizes of the interrogation area in x and y direction respectively and l_z is the light sheet thickness. The effective number of particles should be over 5, see Figure 2.10.

N can be increased by reducing the time interval, but this will affect the dynamic velocity range, which will be explained in the next section. A larger IA can also increase the N, but this will result in a coarser resolution.

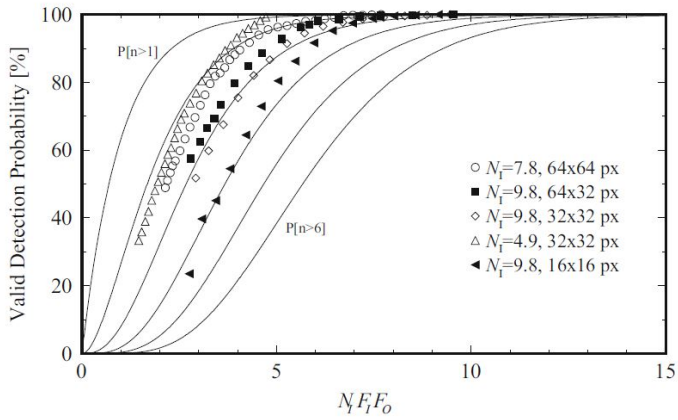

Figure 2.10: The detection of particles in relation to the effective amount of particles (N = N_1 F_1 F_0) [3]

Dynamic velocity range and dynamic spatial range

Reducing the time interval, Δt, will increase the relative uncertainty, $\sigma_{\Delta \mathbf{D}_1}/\mathbf{D}_1$. $\sigma_{\mathbf{D}_1}$ is the precision in locating the maximum peak in the correlation plane for an interrogation window, and $\mathbf{D}_1$ is the displacement. To reduce the relative uncertainty to its previous value, the maximum allowed displacement must be decreased. As a consequence, the dynamic velocity range (DVR), defined in Equation 2.19, will be decreased. DVR relates the maximum allowed velocity to the minimum solvable velocity, and this should be maximized in order to increase the solvable velocity range.

$$DVR = \frac{D_{1max}}{\sigma_{D_1}} = \frac{||\mathbf{V}_{max}||M}{\sigma_{\mathbf{V}\cdot M}} \tag{2.19}$$

The scalar $||\mathbf{V}_{max}||$ denotes the real maximum allowed solvable velocity of particles inside the interrogation area. The reason why the two expressions in Equation 2.19 are equal, is because the time interval (Δt) is a fixed value.

Another important measure is the dynamic spatial range (DSR), which is the ratio of the sensor size to the size of an interrogation window. If the

DSR is too low, small spatial scales can not be solved. Other than increasing sensor size and decreasing the interrogation area, one method to solve this problem is to magnify the image system, e.g. by zooming the lens of the camera.

Optimizing the particle diameter

To minimize the uncertainty, an optimization of the particle image diameter should be analyzed, i.e. the number of pixels that are illuminated by a single particle. The uncertainty decreases with the diameter to a certain number, until it increases yet again. Therefore, the minimum should be identified. From Figure 2.11, one can see that a minimum of 2 pixels should be ensured. This is related to peak locking.

Peak Locking is a systematic error that occurs when the sensor struggles to see the intensity distribution since it is distributed on a small amount of pixels. The measurement will then often conclude that the displacement of particles is valued as an integer, which can be a major source of error. A PIV measurement with peak lock errors is illustrated in Figure 2.12.

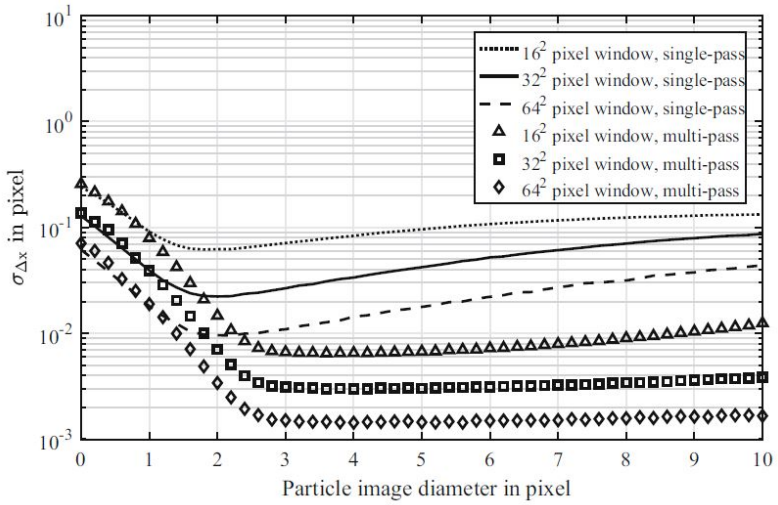

Figure 2.11: The uncertainty in relation to the particle image diameter for different evaluation schemes [3].

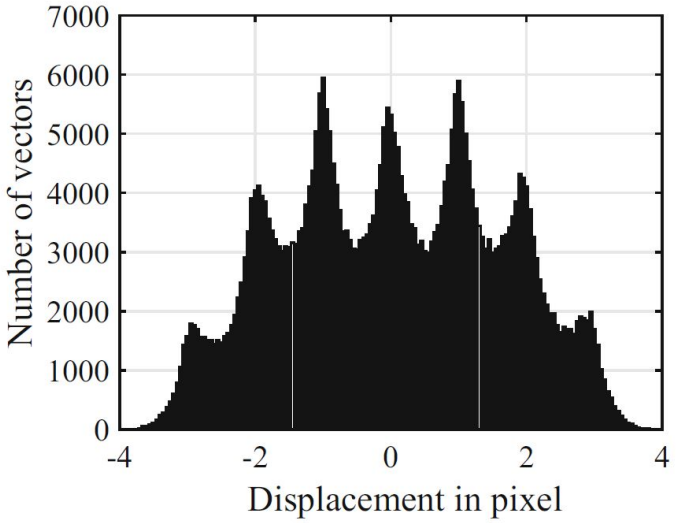

Figure 2.12: A histogram of number of displacement vectors on different displacements, showing the effect of peak locking [3].

Background noise

The background noise should be minimized. A measure of the degree of background noise is the Signal-To-Noise ratio (SNR), and it can be calculated using Equation 2.20.

$$SNR = \frac{\sigma_A}{\sigma_n} = \frac{I_0}{2\sigma_n}\sqrt{N_{ppp} \cdot (\frac{\pi}{4} d_{ppd}^2 - 1)} \tag{2.20}$$

where σ_A is the light intensity of a noise free image, d_{ppd} is the particle image diameter, σ_n is the light intensity of noise in an image and N_{ppp} is the number of particles per pixel. Note that a higher density of particles gives a better SNR.

Curvature of streamlines

One source of error that can not be neglected in turbulent flow is big velocity gradients that introduce curvature to the streamlines. This can in some ways be solved by image deformation, as discussed in subsection 2.2.4, but not always. In that case, smaller Δt or magnification can be good options.

Chapter 3

Literature Review

This chapter will cover relevant literature on turbulent flow that is relevant for the FishPath project. A project thesis was written to prepare for this thesis, where different flows, as well as options to modify them, were investigated for different shapes [1]. Based on the work of Cotel and Webb [20], relevant parameters influencing fish migration were chosen.

- Frequency of vortex shedding
- Size of vortices
- Velocity in wake
- Circulation and vorticity
- The degree of turbulence
- Maintaining a stable vortex shedding regime
- Orientation of vortices

These parameters were investigated on cylinders with circular, triangular and square cross sections as well as wing tips and delta vortex generators in a literature review. With further development in the FishPath project, some modifications have been made. The shapes relevant for experiments will be a short cylinder with a D-shaped cross section, a short cylinder with a triangular cross section and a delta ramp vortex generator. The project thesis investigated two-dimensional (2-D) flow, but for these shapes, the three-dimensional (3-D) effects will be more dominant because of their height. It is still relevant to investigate 2-D effects because they will still appear in the

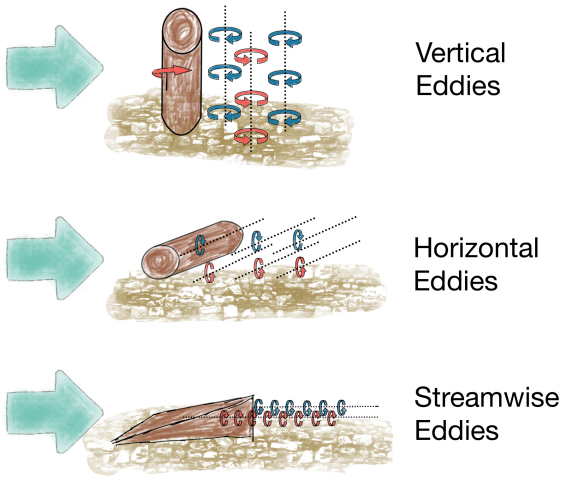

Figure 3.1: Streamwise, horizontal and vertical vortices. Drawing by Bjørn Winther Solemslie.

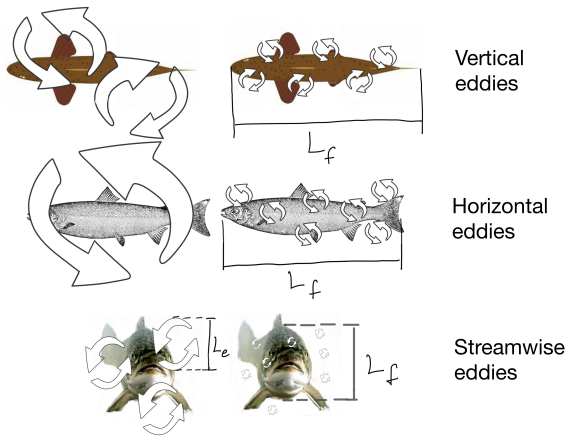

Figure 3.2: Streamwise, horizontal and vertical vortices affecting fish. L_f and L_e is the length scale of a fish and an eddy respectively. Drawing by Bjørn Winther Solemslie.

3-D wake. The shapes will create different properties in their wake and this can be related to how the fish react to each of them. Experimental studies

will be used in this literature review if found. If not, CFD studies can be used as a valuable tool for increasing the knowledge of wakes behind different shapes. The orientation of the vortices can be streamwise, horizontal and/or vertical, see Figure 3.1, and these affect the fish in different rotations, see Figure 3.2.

3.1 The wake behind an infinitely long cylinder with triangular cross section

One part of the results from the literature review in the project thesis are summarized in Table 3.1 [1]. The results do not give perfectly defined variables. This is difficult to achieve due to the complexity of the near wake behind bluff bodies. It is not possible to find an analytic solution, and the structure of the wake is dependent on the specific Reynolds number (Re) and other flow properties of the free stream. There are still some conclusions that can be drawn from this. To achieve periodic solid vortex shedding, a certain range of Re should be ensured [6], see Table 3.1.

The mean velocity in the far wake slowly increases towards the free stream velocity and the wake width slowly increases downstream. The wake width will start as the size of the object because the wake is formed by the shear layers from the separation of boundary layers on the objects. The mean velocity and the wake width in the near wake are complex and difficult to predict. The velocity will have a minimum close to the object and then a more rapid increase. A typical velocity streamwise evolution is depicted in Figure 3.4. Here one can see that there exists some elements of back flow near the object. This is typical for the recirculation area. This area is entrained by the shear layers of each side of the object before they merge and start producing a more chaotic wake. Inside the recirculation zone, there is low pressure compared to the freestream, especially on the surface of the bluff body. Because of the low pressure at the surface, the recirculation zone often has two vortices standing at the same location, i.e. not shedding. Right after the merge of the shear layers, it might take some short distance before vortices start shedding downstream [4]. This is illustrated in Figure 3.3. The evolution of the wake width in the near wake does not have a set shape and can vary depending on the shape of the body.

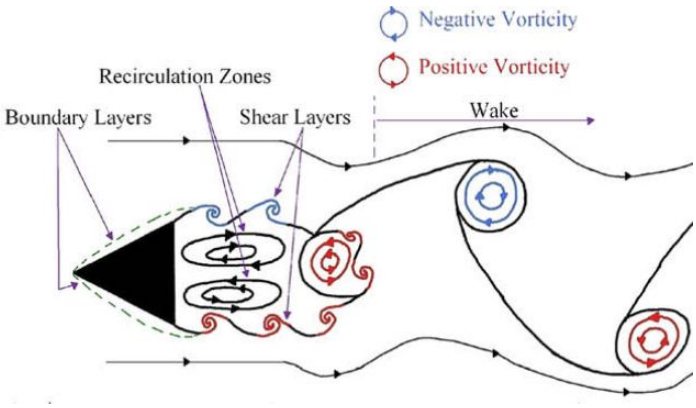

Figure 3.3: Schematic of the near wake [4]

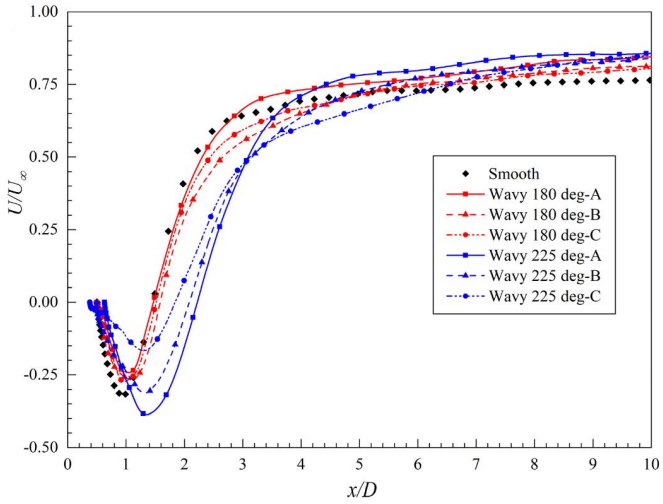

Figure 3.4: The evolution of velocity in the streamwise direction in the near-wake of different cylinders from CFD simulations. The cylinders have been rotated to a different degree around its axis, and A, B and C have different types of wavy patterns [5]

Table 3.1: Vortex tuning for a cylinder with triangular cross section. This is taken from literature and is relevant for 2-D flow. The results have a variable degree of precision as indicated in the table. The table is part of the result from the project thesis written by the author [1]

Vortex variable	**Description**
Stable flow regime	Derakhshandeh and Alam [21] keep the limits for cylinders with triangular and square cross-sections the same. Regular vortex shedding for a circular cylinder: 300 < Re < 1.5e5 and 3.5e6 < Re [6].
Size	The wake width behind objects is the same as the object. It will then grow which can not be perfectly quantified until $U_s/U_\infty < 0.1$. Then $l \sim x_1^{\frac{1}{2}}$ [17]. The vortex diameter is approximately half of the wake width, given a stable vortex shedding regime.
Circulation	Close to a circular cylinder, 1.75 < Γ / (u D) < 3.2, and then the circulation decreases downstream [6]. This makes the diameter a variable to modify to change the circulation. A square cylinder have been found to increase circulation by 60% compared to a circular cylinder, a triangular even more. Vibrating the cylinder can also increase the circulation.
Frequency	Use empirical values for the Strouhal number for the shape and flow condition of interest, and modify the frequency by changing shape or characteristic length, see Figure 3.5 and Equation 2.7. Another tuning option is yawing the cylinder using $f(\theta) = f(\theta = 0)\cos(\theta)$, where θ is the yaw angle [6].
Velocity and lifespan	The streamwise velocity will have a decrease in the near wake and then quickly increase. In the far wake, the wake width follow planar asymptotic wake theory [6], i.e. $U_s \sim x^{-\frac{1}{2}}$ [17]. The vortices will loose their circulation in the streamwise direction.
Orientation	Can make horizontal and vertical vortices.

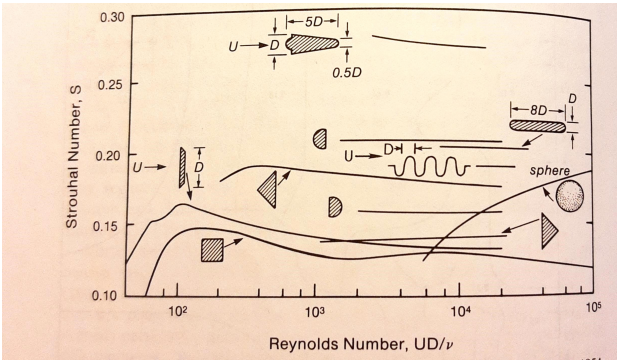

Figure 3.5: Empirically found Strouhal numbers for different shapes [6].

The frequency can be predicted by using Equation 2.7 and Figure 3.5. The circulation is discussed in the circulation row in Table 3.1.

3.2 The wake behind an infinitely long cylinder with D-shaped cross section

Table 3.1 shows results that have many similarities to the cylinder with a D-shaped cross section. The frequency can be calculated by identifying the D-shape in Figure 3.5 and using Equation 2.7. Derakhshandeh and Alam [21] keep the same Reynolds number range as the circular cylinder for keeping a stable flow regime with strong shedding for triangular and square cross-sections. This implies that a the cylinder with the D-shape will have a range similar to that of a cylinder, however this has not been confirmed. Feshalami et al [22] point out that the range defining different flow regimes is made from a circular cylinder so different geometries, 3-D effects and surface roughness can alter this range of Reynolds numbers. The separation point of the cylinder with a D-shape will not be as Reynolds number-dependent as a circular cylinder due to the fixed separation point at the downstream side of the cross section of practically all Reynolds numbers.

The far wake will also follow the asymptotic wake theory as discussed in subsection 2.1.3. In the near wake, it is again hard to predict due to its complexity, but a velocity minimum will appear near the object, as seen in Figure 3.4. From literature, it is hard to predict how this shape compares to cylinders with circular or triangular cross sections. Kazid et al [7] indicate

that the D-shaped cylinder have a smaller region of low velocity than a circular cylinder in their 2-D CFD simulation. They also show that it has a higher vorticity than cylinders with circular and square cross sections, but not as high as the triangle, see Figure 3.6. This needs verification, hence more CFD simulations and experiments are needed for more detailed descriptions and for a larger range of flow properties. The orientation of the D-shaped cylinder can create horizontal and vertical vortices.

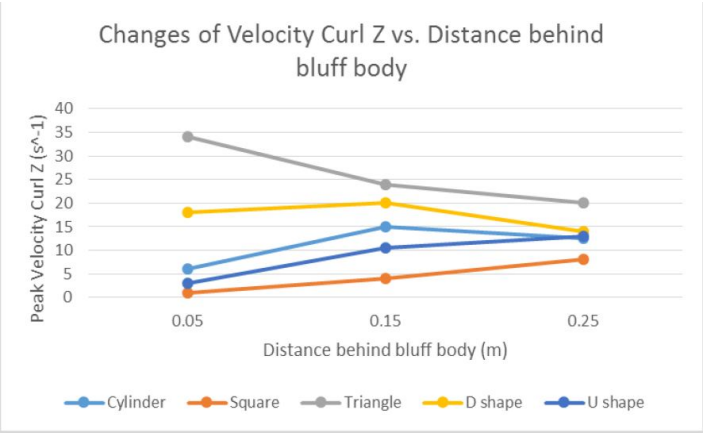

Figure 3.6: Evolution of the z-component of vorticity in air in the streamwise direction. Re = 5000. The results are from CFD-simulations [7].

3.3 Three dimensional flow effects

If the height of the shapes discussed previously is reduced, the wake will deviate from 2-D flow. This is due to end effects. The aspect ratio (AR) of a circular cylinder is defined as the length over diameter, and as AR decreases, the more dominant the 3-D effects will become.

Uffinger et al [23] mention four types of vortices in the near wake of a finite cylinder mounted on a ground plane, and they are depicted in Figure 3.7. The horseshoe vortices form at the ground plane and travel around the cylinder, forming a horseshoe structure. These vortices are negligible in the analysis of Uffinger. The base vortices form on the ground plane near the cylinder. These streamwise vortices on each side of the cylinder rotate with different signs, and create an upwash. This upwash is especially applicable when AR is big and the boundary layer (BL) is thick [24]. The tip vortices

at the top of the cylinder are also streamwise, but create a downwash force, forcing the flow downwards. If AR is reduced, the downwash increases [9]. In the middle of the cylinder, the classical 2-D flow discussed in the previous sub sections appears. When AR gets small enough, the tip vortices react with the 2-D flow and create an arch like structure, see Figure 3.8. In this figure, Wang [8] distinguishes between a symmetrical vortex pair that forms with low AR, and an asymmetrical vortex pair that forms with larger values of AR. Uffinger points out that 3-D flow of finite cylinders are inherently complex and can vary as flow properties vary. Predicting flow in the near wake is therefore very difficult to accomplish.

Another 3-D effect is what is known as the backward-facing step flow, see Figure 3.9. When there is a flow over a surface that creates a step, a shear layer creates forces inwards to the downstream side of the structure. This region have low pressure and can create a type of recirculation [10]. This effect can be evident in vortex generators, especially those with low AR.

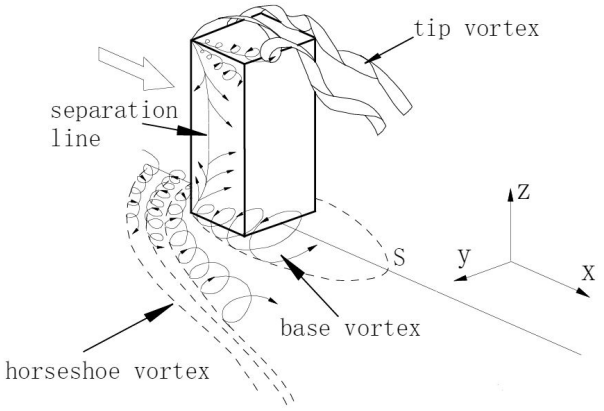

Figure 3.7: Vortices in the near wake of a finite square cylinder [8].

Park and Lee [25] have done experiments as well as a literature review on the 3-D effects of finite cylinders, where they mention that the regular and strong vortex shedding stops at AR<7 for Re = 15 000 [26]. Vortex shedding is largely dependent on AR in general [27]. From the experiments, they found that the vortex formation region is elongated (in the near wake) and the shedding frequency is decreased when AR is decreased. The 3-D effects are mainly due to downwash from the vortices separated from the

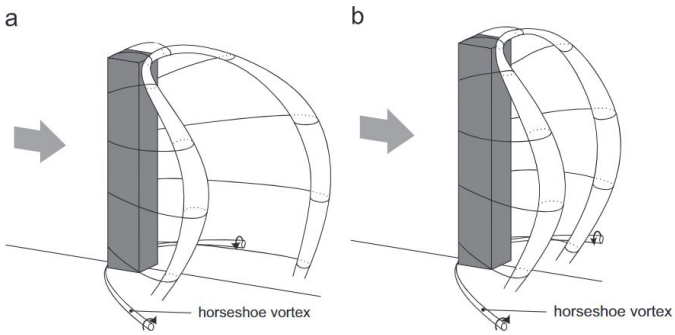

Figure 3.8: Vortices in an arch like structure of a finite cylinder [9]

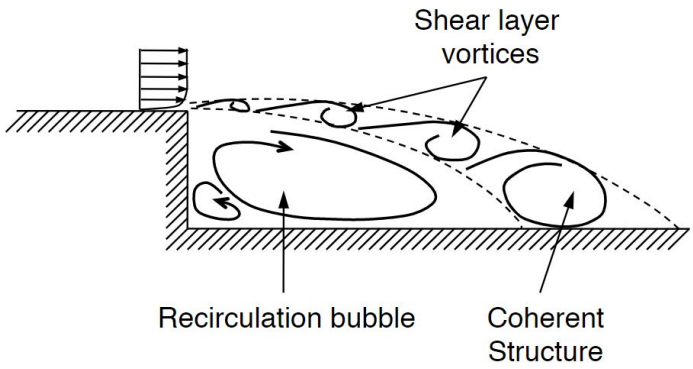

Figure 3.9: Backward-facing step flow effect [10].

free end.

Okamoto and Yukisada [28] writes that the vortices shed are more symmetrical for AR = 1-2 than for longer cylinders that have more asymmetric vortices. The Strouhal number decreases as AR increases up to AR = 3-4, and increases after that. Furthermore, the turbulent eddies tend to enlarge near the free end, especially for symmetric vortices. Away from the free end, the rate of decay of turbulent eddies is rapid, especially for asymmetric shedding. The turbulent eddies enlarge downstream of the wake. The effect of downwash is significant for AR = 1-2, and the z-component for turbulent intensity is greater than the x-component, so the wake will expand in the vertical direction.

3.4 Wake behind a delta ramp vortex generator

The literature on vortex generators are mainly studying the ability to delay separation. Therefore, studies on vortex generators of scales that are larger than boundary layers are often lacking. A delta micro ramp is a vortex generator in the shape of a backwards delta wing, see Figure 3.10.

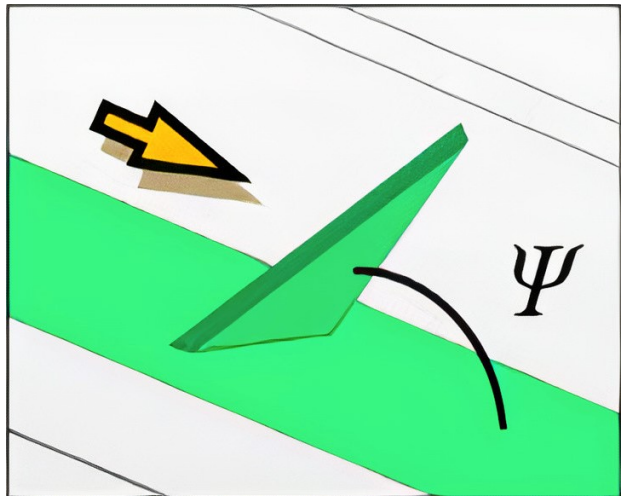

Figure 3.10: A delta ramp vortex generator [11]. Ψ is the angle between the tip of the ramp and the ground.

The delta ramp is chosen because it creates streamwise vortices, and as opposed to the delta wing, it does not catch objects from a flow. One problem with the analysis of the ramp is that its purpose is most often in literature used to control shock wave boundary layers [29]. Supersonic flow is not comparable to subsonic flow which is the scope of this thesis.

There exist some literature that investigates the micro ramps for enhancing heat transfer in heat exchangers with subsonic gas. Ogawa and Usui [11] show with CFD that the pressure drop behind the ramp increases with the increase of the angle up to 90 degrees, see Figure 3.10. They also show that they create two streamwise vortices, but they quickly disappear, as seen in Figure 3.11. It is also evident that the vortices are weaker than those from a delta wing vortex generator.

For the wake behind a ramp that is more relevant to the scope of this thesis, CFD and experiments for this specific project are needed. CFD sim-

ulations done for the FishPath project will follow next.

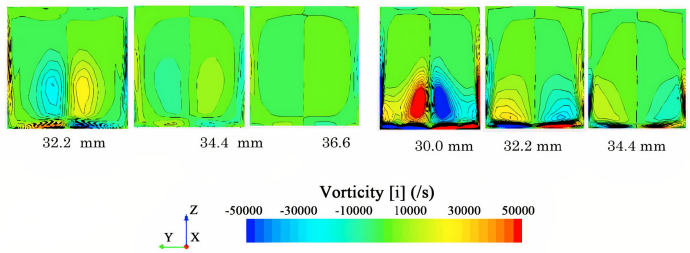

Figure 3.11: Vorticity from ramp. The three pictures to the left shows the vorticity from a 45deg ramp, and the pictures to the right shows the vortices behind a 135deg ramp, i.e. a delta wing [11].

3.5 CFD results

In this literature review, the diameter of the cylinder with isosceles triangular cross section is defined as the long side of the triangle and the flow behind the appendices is taken at a plane 50% of the height of the appendices. In the methodology and the following results from PIV and CFD in this thesis, the diameter of the cylinder with triangular cross section is defined as the short sides and the flow is taken at 62% of the height of the appendices. In both cases, the characteristic length for determining Reynolds number, is defined as the long side.

CFD simulations have been done for the FishPath project by SINTEF. It is important to note that this is not published research, and the results have not been validated yet. The shapes (hereby named appendices) and velocities are decided in FishPath meetings, and have been modified as the project moves forward. The three appendices are a short D-shaped cylinder, hereby denoted D-cylinder, a short cylinder with a triangular cross section, hereby denoted spear, and a delta wing vortex generator mounted to a hydrofoil. The hydrofoil is a NACA0006 foil. The appendices are depicted in Figure 3.12. They have a low AR, somewhere between one and two. The data that will be presented here are acquired from a plane at 50% of the heights of the appendices.

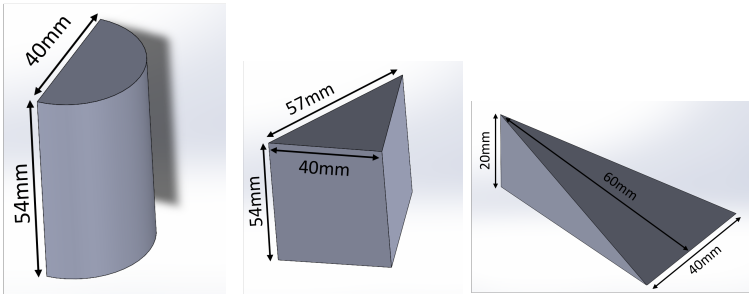

(a) The D-shaped cylinder

(b) The spear

(c) The delta ramp vortex generator

Figure 3.12: The appendices used in the CFD simulations.

		D-cylinder (Re = 10E+3)			**Spear (Re = 14.25E+3)**		
		ω_x (1/s)	ω_y (1/s)	ω_z (1/s)	ω_x (1/s)	ω_y (1/s)	ω_z (1/s)
2D	Max	12.05	35.27	8.40	8.01	34.35	2.25
	Min	-9.52	-27.71	-12.65	-6.86	-29.70	-13.37
12D	Max	6.39	6.54	3.16	5.46	9.09	4.34
	Min	-5.18	-5.97	-5.25	-9.12	-8.40	-5.62

		D-cylinder (Re = 40E+3)			**Spear (Re = 57E+3)**		
		ω_x (1/s)	ω_y (1/s)	ω_z (1/s)	ω_x (1/s)	ω_y (1/s)	ω_z (1/s)
2D	Max	65.74	99.20	49.64	53.10	131.69	15.57
	Min	-86.68	-112.09	-58.37	-55.48	-112.09	-55.62
12D	Max	26.10	20.89	11.57	20.32	27.41	15.47
	Min	-15.47	-17.31	-15.09	-22.71	-25.56	-18.27

Table 3.2: Values of instantaneous vorticity components (ω) in the wake of the D-shaped cylinder and the spear. CFD simulations by Marcell Szabo-Meszaros (SINTEF)

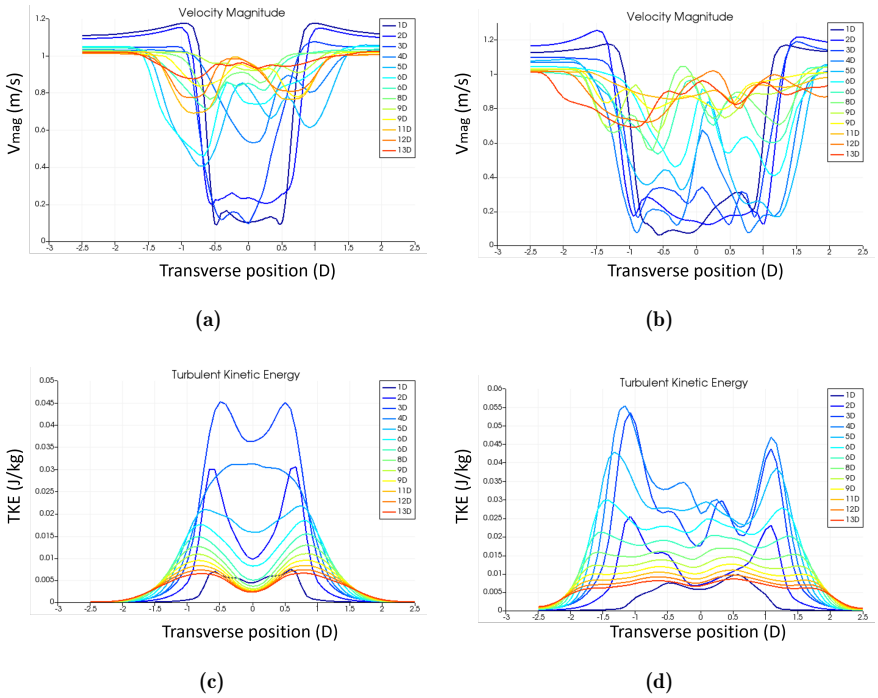

Figure 3.13: Velocity and Turbulent Kinetic Energy (TKE) plot of the wakes behind the a) & c) D-cylinder (Re = 40 000) and b) & d) spear (Re = 57 000) respectively. CFD simulations by Marcell Szabo-Meszaros (SINTEF)

As discussed in section 3.1, one can see from Figure 3.13 that a velocity deficit is formed in the near wake, where the velocity magnitude is lowest in the near wake, and then rapidly increases downstream. This yields for the D-cylinder and the spear. The spear have a wider wake by observing the fact that the wake grows in the transverse direction more quickly than the D-cylinder in Figure 3.14. Here, vortex shedding is observed, and the shedding starts earlier for the D-cylinder than for the spear.

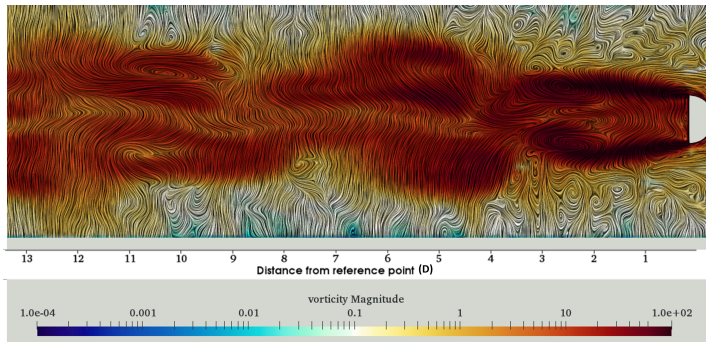

(a)

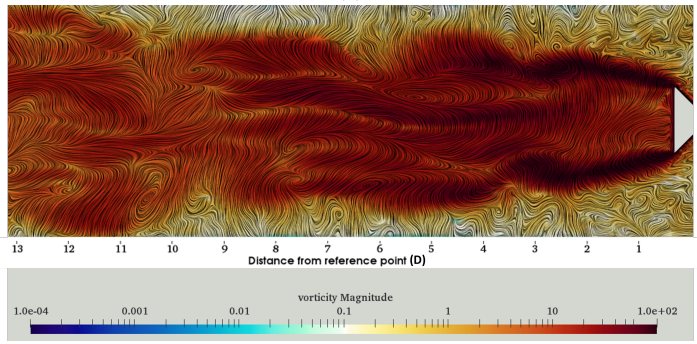

(b)

Figure 3.14: Vorticity plot of the wakes behind the a) D-shaped cylinder (Re = 40 000) and b) spear (Re = 57 000). The data is taken from the xy-plane at 50% of the vertical height of the appendices. CFD simulations by Marcell Szabo-Meszaros (SINTEF)

If the shapes were infinitely long, the flow would have 2-D flow characteristics, and the only noticeable vorticity would be the ω_y. In this case, Table 3.2 demonstrates that the wake includes noticeable vorticity components in both the z and x directions, indicating significant 3-D effects, as discussed in section 3.3. The y-component of the vorticity is still dominating the wake, so there are 2-D effects present as discussed in section 3.1 and section 3.2. Comparing the low Reynolds number flow to the high Reynolds number flow in Table 3.2, the vorticity clearly grows with bigger Re. Since the simulations of the two shapes do not have matching Re, the similarites can not be exactly identified, but the vorticity of the two components is somewhat similar. Using Equation 2.2, Figure 3.6, the results from Table 3.1

and the fact that the spear has a slightly wider wake, one can argue that the spear have a bigger circulation than the D-cylinder. Note that the vorticity results from the simulation are instantaneous measurements, so the result may be dependent on when in time it is taken from.

As seen in Figure 3.13, the turbulent kinetic energy (TKE) is steadily decreasing downstream for both the spear and the D-cylinder. They both have spikes on each side of their wakes, with low TKE at the center line (y = 0). TKE distribution is more chaotic and uneven in the spear than in the D-cylinder. It also has a wider spread, indicating that the wake behind the spear is larger.

As discussed in section 3.4, the delta ramp is expected in literature to produce two streamwise vortices. The vortices are also expected to lose their vorticity quickly downstream. Since streamwise vortices are expected, the biggest vorticity component should be ω_x which Table 3.3 shows for Re = 40E3, but not for Re = 10E3. A proper size of the Reynolds number must therefore be ensured. The two primary vortices have broken down at 12D downstream. Figure 3.15 shows that the wake forms a velocity deficit that is largest right behind the two vortices. The velocity deficit is small close to the ramp, grows quickly after the first couple of diameters downstream, and then decreases again at roughly 5–6D downstream. The TKE is steadily increasing downstream until 12D. The production of turbulence must come to an end at some point, and it is assumed from these simulations that this happens further downstream, but these results require validation. The TKE is greatest at the location of the vortices.

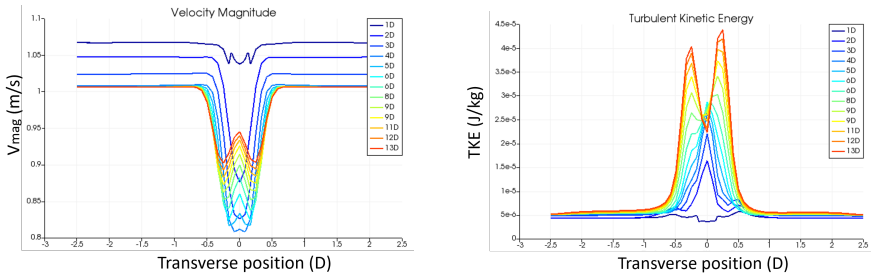

(a) (b)

Figure 3.15: a) Velocity and b) Turbulence Kinetic Energy (TKE) plot of the wakes behind the delta ramp vortex generator (Re = 40 000). CFD simulations by Marcell Szabo-Meszaros (SINTEF)

		Ramp delta VG (Re = 10E+3)			**Ramp delta VG (Re = 40E+3)**		
		ω_x (1/s)	ω_y (1/s)	ω_z (1/s)	ω_x (1/s)	ω_y (1/s)	ω_z (1/s)
2D	Max	3.94	9.25	4.14	72.92	34.98	17.20
	Min	-13.93	-9.30	-6.04	-72.75	-34.61	-16.97
12D	Max	3.57	4.62	2.34	15.03	13.69	6.31
	Min	-3.64	-4.91	-2.66	-14.93	-14.02	-7.24

Table 3.3: Instantaneous vorticity components for the delta ramp vortex generator. CFD simulations by Marcell Szabo-Meszaros (SINTEF).

Chapter 4

Method

This chapter will cover preparation for the experiments in the water channel to come after this thesis is written, as well as the methodology for the PIV measurements done in the smaller test rig.

4.1 Preparation for experiments in the water channel

The water channel at NTNU has a cross section of 1m x 1m, and can pump water up to $1m^3/s$. A drawing of the channel can be seen in Figure 4.1. The channel is not transparent, and will therefore not have optical access in two directions perpendicular to each other, which is required for PIV, as discussed in section 2.2. A solution to this is conceptually illustrated in Figure 4.2. This requires a rig that is specially designed for the water channel. The design of the experimental rig can be seen in Figure 4.3. This rig will facilitate that optical equipment can access a new point of view in a dry environment.

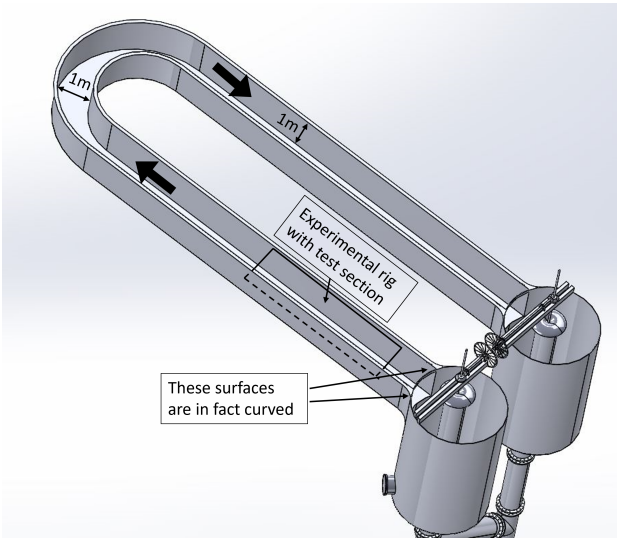

Figure 4.1: Modified from water channel CAD-drawing by PTM industries for the Waterpower Laboratory at NTNU.

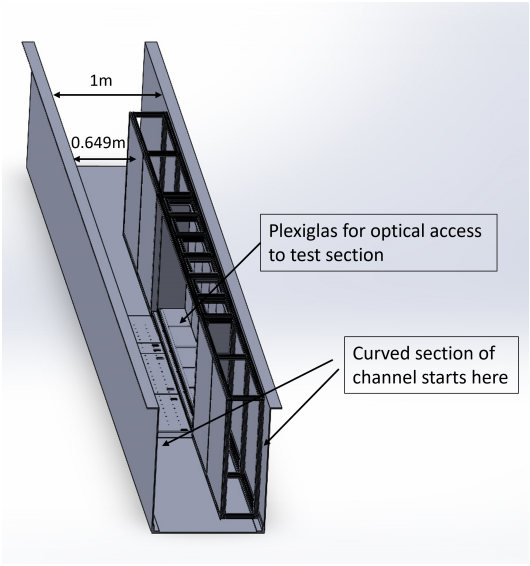

Figure 4.3: Experimental rig in the water channel. The rig will be mounted on top by Aluflex-installations transversely. Drawing by PTM Industries for the Waterpower Laboratory at NTNU

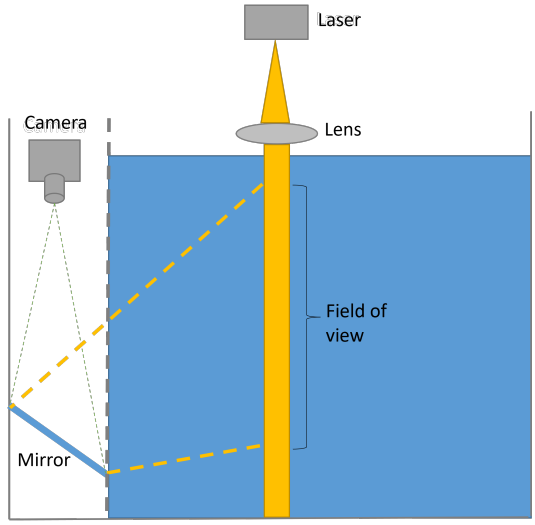

Figure 4.2: Conceptual drawing of PIV in the water channel, taken from the project thesis of the author [1].

In the transition from the walls of the channel to the circular tanks, there are curved surfaces, which the drawings of the channel do not show. To obtain a symmetric inlet flow, a block placed in the transition between the experimental rig and the tank was designed, see Figure 4.4. The block needed to fit the curved surface of the channel.

As discussed in the project thesis of the author [1], the design of a water channel is comparable to the design of a wind tunnel in many ways [30], so the following citations are from wind tunnel literature. In articles where a water channel for experiments are designed, they often reference wind tunnel literature (e.g. [31], [32]). The start of the inlet will experience turbulent eddies in the transition from the tank to the channel. Therefore, a honeycomb was designed to straighten the flow and decrease eddies, or more specifically, lateral components of turbulence [33]. By introducing a construction with cells, the turbulent eddies will be divided into eddies with the size of the cells, and the goal should ideally be eddies in the integral length scale [34], as described in subsection 2.1.2. This length scale is not known, so the cell size must be decided in another way. The optimum cell size is not defined in literature, and the cell size is not the most crucial part of designing a flow straightener [33], [34], [35]. Ideally, small cell size but big porosity (β,

i.e. area of flow to total test sectional area ratio), where Mauro et al [35] suggest not subceeding 80%. A more important parameter is the length to cell diameter ratio, which should ideally be between 6 and 8.

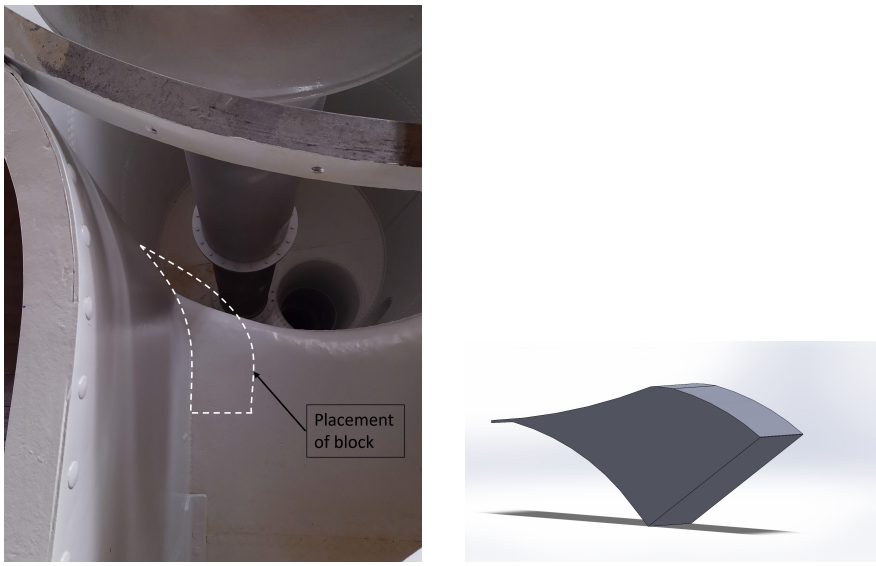

(a) a **(b)** b

Figure 4.4: a) Picture of the transition between the inlet tank and the water channel b) Design of a block that will act as a transition between the tank and the experimental rig to achieve symmetrical inlet conditions.

A suggested design can be seen in Figure 4.5. Cells in a hexagon shape have been chosen because they have a shape with big porosity. A cell size of 14mm, a wall thickness of 1mm and a length of 8.4cm are proposed for the design of the honeycomb. This results in a length to cell diameter of 6 and a porosity of 89%. The foundation for this calculation can be seen in Appendix B. The material should be chosen based on the ability to hold a water flow of $2m/s$ with the chosen wall thickness. The cell size, cell shape, wall thickness, length and material can be changed based on what manufacturers have in stock with the previous analysis in mind. In addition to a honeycomb, one or multiple screens should be added downstream to reduce streamwise velocity fluctuations. The porosity of screens should be 58%-80%, and can have a square mesh [35].

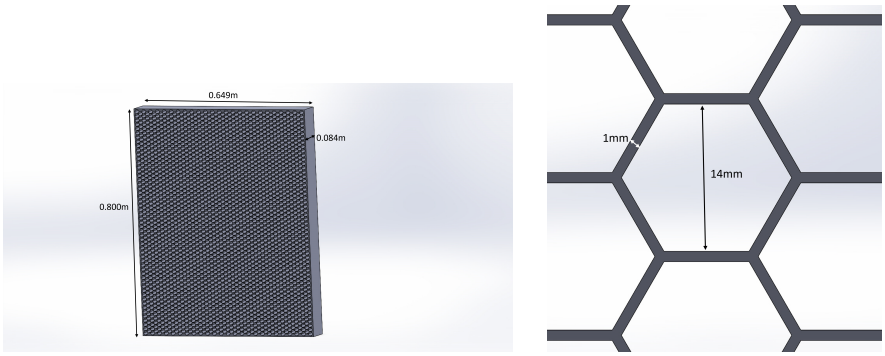

(a) (b)

Figure 4.5: a) Design proposal for a honeycomb b) Design of the hexagonal shape of the cells in the proposed honeycomb design.

4.2 PIV measurements in the test rig

PIV measurements have been conducted at the Waterpower Laboratory in a test rig, to study the wake behind the spear mounted on a hydrofoil. Descriptions of the test rig, spear, PIV set up and systematic error analysis will be described here.

4.2.1 Test rig

PIV measurements were conducted in a smaller experimental rig compared to the water channel, see Figure 4.6. The camera and laser have optical access through Plexiglas mounted to the test rig. This area can easily leak if not mounted carefully, so the glass and the full water way were closely inspected for leaks. The planar test section for measurement is 100mm x 77mm and the height of the test section is 150mm but is divided by a hydrofoil where an appendix is mounted on top. The hydrofoil deviates from the NACA0006 foil in the CFD simulations. The hydrofoil in the test rig is custom made, with a one degree downward slope downstream and a symmetric trailing edge for the last 12.5mm. The water will run through a closed loop, and a tracing particle feeder is connected to the loop with an electronic valve connected to LabView.

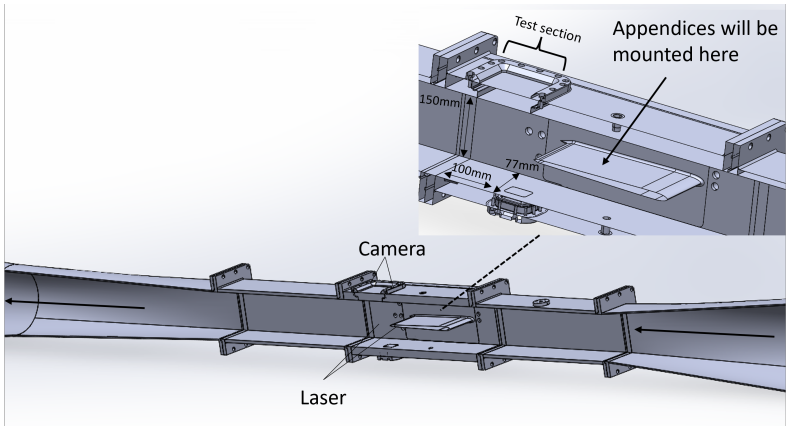

Figure 4.6: Test rig. CAD drawing by PTM industries for the Waterpower Laboratory and modified by Kristian F. Sagmo.

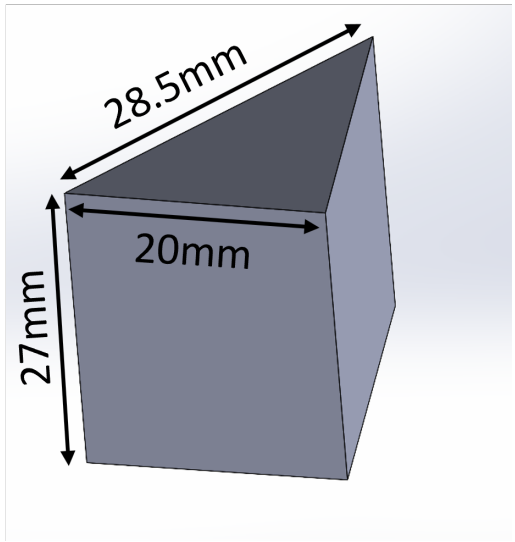

Figure 4.7: The spear that was printed, and will undergo measurements. The diameter of the spear is defined as the short side of the triangle, i.e. 20mm.

The size and placement of the spear were chosen based on achieving a geometrically similar shape as well as having the same Reynolds number

as the CFD simulation with the highest Reynolds number as described in section 3.5. The size of the spear was also chosen to achieve a blockage effect subceeding 7.5%. The blockage ratio is defined as the frontal area of objects to the cross sectional area, and if it exceeds 7.5% the walls will adversely affect the flow [15]. The spear can be seen in Figure 4.7, and further descriptions of the placement can be found in Table 4.1. A non-dimensionalized figure comparing the spear on the hydrofoil with the PIV and the CFD simulations can be seen in Figure 4.8. Note that there will be walls in the test rig, but not in the simulations. Even with the blockage ratio consideration, the walls will still affect the flow. The diameter is defined here as the short side of the triangle, i.e. 20mm and 40mm for the PIV and the CFD respectively. The spear was printed in PLA, triple coated and attached with two component epoxy glue to the hydrofoil, 35mm upstream from the trailing edge.

Table 4.1: Parameters for the spear that in PIV measurements and from the CFD simulations

	PIV	CFD
D (mm)	20	40
$\mathbf{V}_{bulk}$ (m/s)	2	1
Re	57 000	57 000
Blockage (%)	7.4%	None
Placement upstream trailing edge (D)	1.75	4
FOV downstream spear (D)	[2.4,4.2]	[0,10]

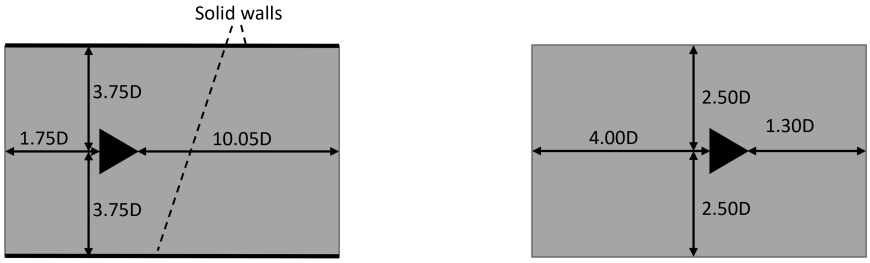

(a) **(b)**

Figure 4.8: The position of the spear on the hydrofoil for a) PIV and b) CFD

4.2.2 PIV set up

A Health, Safety and Envionment (HSE) analysis was done because this experiment involved a class 4 laser. The HSE form can be seen in Appendix D. A tent was built around the test rig to shield out reflections from the laser beam as a safety measure. A power unit, which powers the laser as well as cooling the system, was placed outside the tent. The laser head was placed inside the tent, and the beams were guided with a guide arm on the side of the rig. The laser is then sent through a laser sheet optic device to generate the laser sheet that will cover the FOV. The tent and the experimental set up can be seen in Figure 4.9. The laser can emit two separate beams to achieve a short time delay between the two laser pulses, and these two beams were adjusted so that they overlapped. To be able to achieve a consistent time delay between the two pulses, a laser timing stabilizer with an optic cable attached to the laser head was installed.

The camera was mounted on top of the rig, achieving a birds-eye view of the test section, perpendicular to the laser sheet. A programmable timing unit was installed to be able to synchronize the laser beams and the camera exposures. The FOV is restricted to 45mm x 36mm by the vertical placement of the camera and the lens available. The vertical height of the camera is restricted because there is a pipe roughly 40cm over the test section. The FOV covers the flow from 47mm to 83mm (2.4D to 4.2D) downstream the spear, and -22.5mm to 22.5mm (-1.1D to 1.1D) in the transverse direction, see Figure 4.10. The vertical placement of the FOV is set to 16.7mm of the 27mm tall appendix. This means that the measurement plane is placed 62% of the height of the spear, unlike the data from the CFD literature review, which is taken from 50% as described in section 3.5. Velocity fields from the CFD simulations at 62% of the height of the spear will be presented in chapter 5. The aperture was set to f/2.8 to achieve a shallow depth, which is needed because the PIV measurement is 2-D.

Two pictures were taken in still water and inspected in DaVis 8.4 to ensure that the laser beams still overlapped. Then, the focus was adjusted and the camera tilted such that it was planar to the test section. A calibration plate was placed in the upstream part of the test section with the system filled with water. Spacing blocks were placed beneath and on the side of the plate to be able to know the location of the plate. Then, the calibration function in DaVis 8.4 was used. Here, the software relates the pixels on the camera sensor to the millimeters on the physical plate, using a 3rd order polynomial fit. The average was 28.6357 pixel/mm and the root mean square error of the fit was 0.47 pixels. This is acceptable because it is small

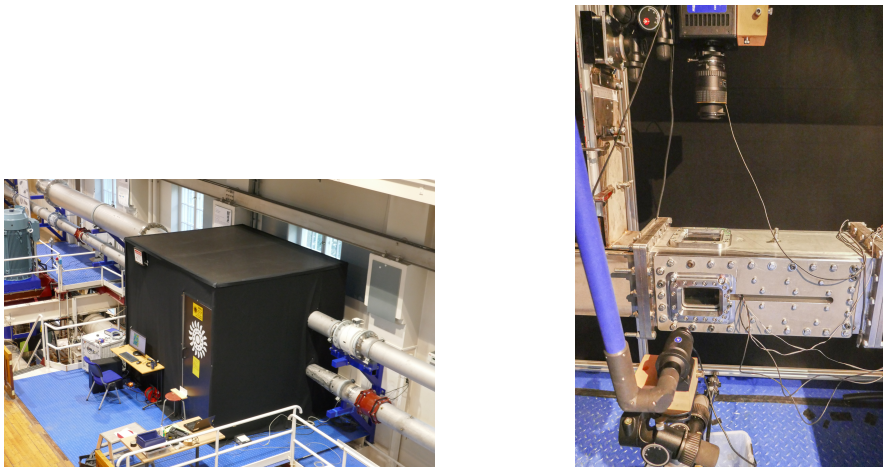

(a) (b)

Figure 4.9: a) The tent built to shield out reflection of the laser b) The test rig with the laser guide arm and camera.

compared to the 1028 x 1290 pixel resolution of the camera. The calibration plate and a snapshot of the calibration window in DaVis 8.4 can be seen in Figure 4.11. The tracer particles were added to the flow. The wavelength of the laser is 527nm, and the particles have a diameter of 9-13μm, which ensures that the particles are easily within Mie scattering as discussed in subsection 2.2.2.

Four measurements were done with a 200Hz image rate and two with 800Hz. Because the maximum image acquisition for the computer used is 4367 images, the 200Hz was slower with a measurement time of 21.8 seconds, compared to the 800Hz of 5.5 seconds. The 200Hz had lower uncertainty. More on that in the next chapter. There were also measures to decrease systematic errors by inspecting some interrogation areas closely. More on that in the next subsection. This analysis resulted in a time between laser pulses of 240μs. The flow rate was read at the flow meter for every measurement. When evaluating the measurements, the multi pass approach was used, which is described in subsection 2.2.4. By pre estimating the displacement with larger interrogation areas, the multi pass algorithm can find a suitable DVR, which the correlation algorithm is capable of calculating. It starts by approximating the displacements in 64 x 64 pixel areas, and results in 50% overlapped interrogation areas of 32 x 32 pixels when finished.

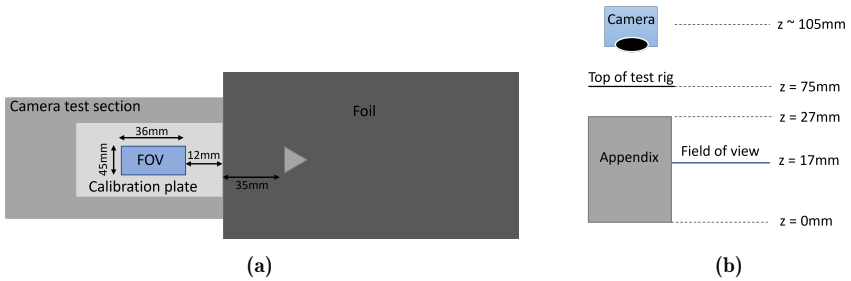

Figure 4.10: Description of the placement of the field of view in the a) xy-plane and b) zx-plane

Table 4.2: PIV parameters

Software	DaVis 8.4
Laser name	Litron LDY300
Laser specifications	527nm wavelength, Nd:YFL dual-cavity
Camera	Photron FASTCAM Mini UX100
Lens	Tokina AT-X Pro 100mm, f/2.8
Laser timing stabilizer	LaVision LTS
Tracer particle	Glass hollow spheres, d_p = 9-13 μm, ρ = 1.1g/cm^3
Camera sensor	CMOS, 1280x1024 pixels
Recording	Double frame, double exposure
FOV	45mm x 36mm (y-x)
Rate of image acquisition	200Hz and 800Hz
Time between laser pulses (Δt)	240 μs
Number of images per measurement	4367
Measurement time	21.8s and 5.5s
IA size before multi pass	64 x 64 pixels
IA size after multi pass	32 x 32 pixels

Deformation of the IA was also performed to account for vorticity and curvature streamlines. When the measurements were finished, the calibration plate was once again placed in the water, and inspected to see if the camera or laser had moved. The calibration plate was in the same place as before the measurements in the FOV. Relevant parameters for the PIV measurements are summarized Table 4.2. When post processing the data, DaVis 8.4 removed spurious vectors, used a background noise filter and did intensity capping.

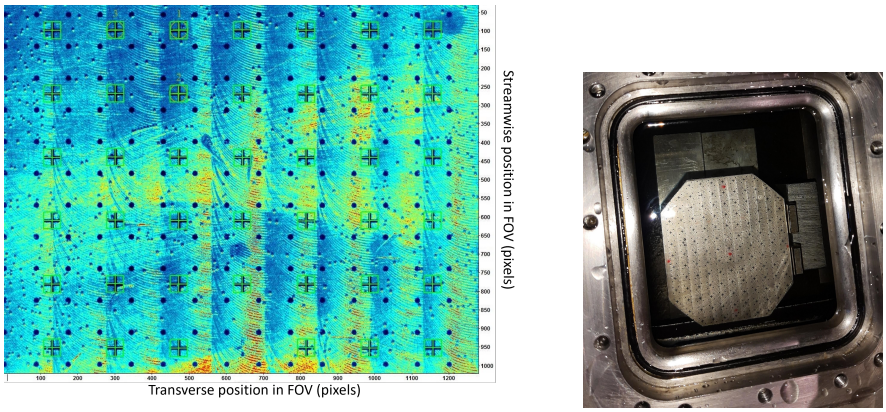

(a) **(b)**

Figure 4.11: a) Picture of the calibration plate in the field of view in DaVis 8.4. b) The calibration plate submerged in water before the lid is mounted.

4.2.3 Systematic error

The systematic error will be discussed here, as described in subsection 2.2.5. The pixel size was ensured exceeding 3, which will not give any noticeable peak locking effects. It was also ensured that there were roughly 10 particles per interrogation area. The effective particle images, which is the number of particles that do not go out of the interrogation areas or the plane, should be over 5. By ensuring roughly 10 particles per IA, as well as displacement of roughly 5-6 pixels, the effective particle images are at a satisfactory level, and the correlation algorithm has good availability of data. This is based on experience of previous experiments done in the test rig. A picture of an IA with particles with satisfying density and size can be seen Figure 4.12.

The water that was used was not as clean as it should be. There were always visible dirt particles in the water. They do not have the good scattering properties as the glass hollow spheres, but it can still mean that the software recognizes them as tracer particles. Hopefully, they follow the flow in the same way as the tracer particles, but they are not made for PIV and the response time may be insufficient for a turbulent flow with rapid fluctuations and vorticity. The water should therefore be cleaned for the next experiments. The fact that the flow is highly turbulent could also affect the tracer particles adversely. There will be a large variation in velocities in the FOV as well as curvature streamlines and circulating flow pushing the par-

ticles in its radial direction. This means that the effective particle images, shift displacement and density will be different depending on which IA that is analyzed.

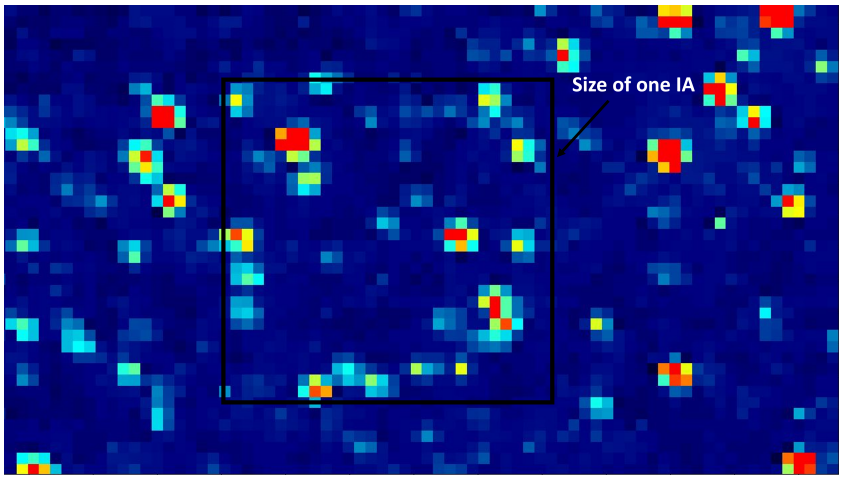

Figure 4.12: Snapshot from DaVis 8.4 of a small area of the field of view. The size of one interrogation area is illustrated.

The hydrofoil that the spear is standing on differs from the CFD, and the placement of the spear on the foil as well, as seen in Figure 4.8. This can have some influence on the result, but the biggest impact will be that the PIV measurement is entrained by walls, while the CFD domain does not. The walls can induce blockage effects that will affect the flow adversely. The materials of the two methods are also not similar, and these should be considered more thoroughly matched next time. The spear was 3-D printed in PLA and coated with three layers, but there was still some small inflation on all surfaces of the spear that changed the shape slightly, meaning that water leaked into the structure. After the PIV measurements, tests were performed to find out if velocity cavitation would occur and how well the glue held with water flow velocities up to 10m/s. It is likely that the leakage through the coating happened at these velocities, but it is not certain. The surface with the most significant inflation is pictured at Figure 4.13, and shows the surface with the largest inflation. This could be a significant systematic error if this was present during the measurements.

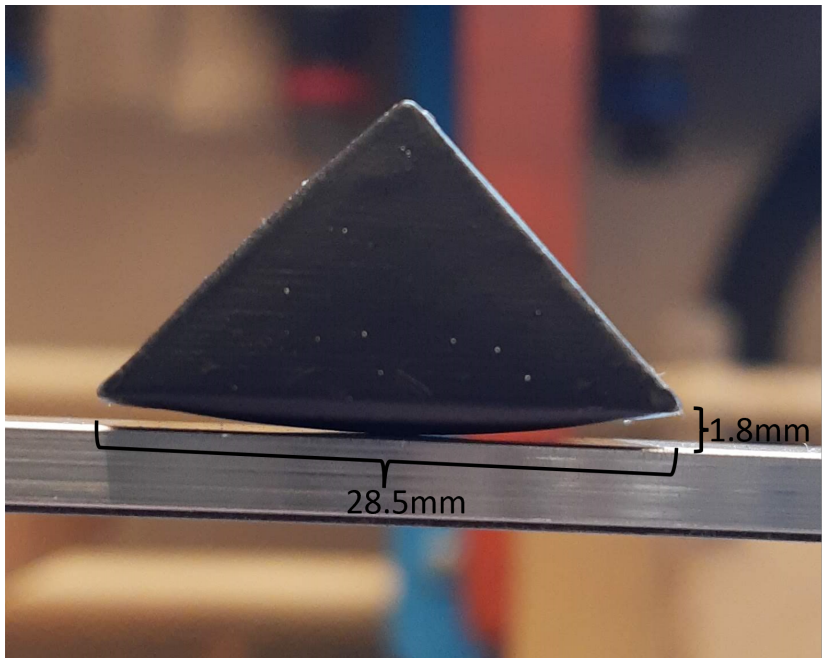

Figure 4.13: Picture of the spear after undergoing measurements and cavitation tests.

Chapter 5

Results and Discussion

5.1 PIV results

Four measurement sets were obtained, and each measurement set with 4367 vector fields was averaged and non-dimensionalized by their respective bulk velocity. Then the four sets were averaged, and the results can be seen in Figure 5.1 and Figure 5.2. The velocity field clearly shows that there are two areas with circulation present. They are roughly symmetrical on the center line (y=0) and show a substantial backflow in these two areas. Moreover, the areas are separated by a flow moving steadily downstream. This deviates from the idealized 2-D recirculation zone, where the two vortices meet in the middle and create back flow, as seen in Figure 3.3. However, there is still reason to believe that this is some form of recirculation area because the velocity does average to this specific back flow, which it would not be if the structures were random or shedding downstream. This is further demonstrated in the vorticity plot of Figure 5.3, which shows the vorticity that is contributing to the backflow. The plot also shows the strong vorticity created at the edge of the image, i.e. the shear layer originating from the separated boundary layer at the downstream part of the spear. The change from the recirculation zone to the wake downstream is sudden and easily seen at roughly 3.6D downstream of the spear. What these results show can be interpreted as the transition from the recirculation zone to the regular wake downstream.

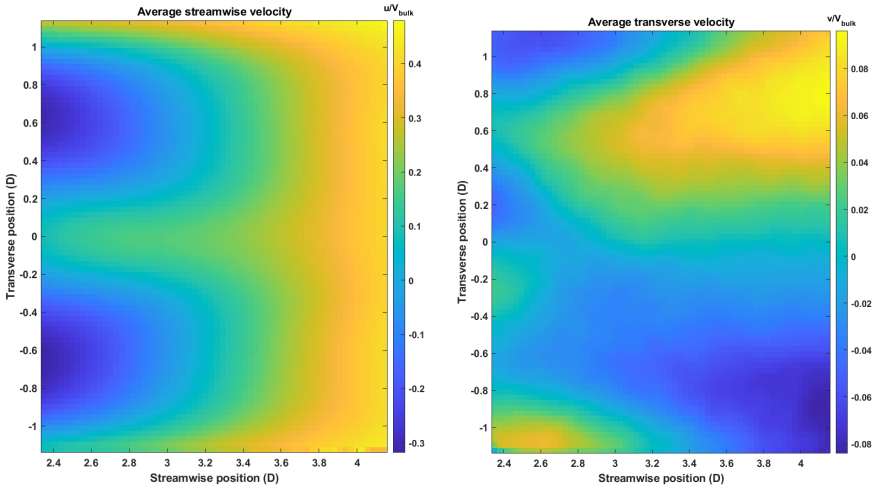

(a) **(b)**

Figure 5.1: Velocity fields obtained from PIV measurements of the a) Streamwise component and b) the transverse component.

The reason for this type of circulation is hard to explain with only one measurement plane. The spear has an aspect ratio smaller than 2, which indicates a flow which is highly affected by 3-D flow effects, as discussed in section 3.3. The measurement plane is placed at 62% of the height of the spear. Here, the flow will be affected by the backward-facing step effects and tip vortices that create downwash. These effects can be part of the force that contributes to the back flow along with the 2-D shear layers. The downwash can also be the reason for the downstream velocity between the backflow regions. The downstream surface of the spear is the long part of an isosceles triangle, which indicates a big surface with low pressure holding the circulation in the recirculation area in place. Together with 2-D flow effects, this complex mix could essentially create the circulation areas that are present in the results. As discussed in section 3.3, there is literature that states that the vortex formation region is elongated and symmetrical for aspect ratios between 1 and 2, and this statement corresponds well with the PIV result. It is also suggested that the vortices formed near the spear have an arc-like structure, but this can not be verified in these measurements. To be able to further validate the suggestions from the literature review, PIV measurements in several planes and/or a stereoscopic PIV are necessary. With only one plane, no conclusion to this can be drawn.

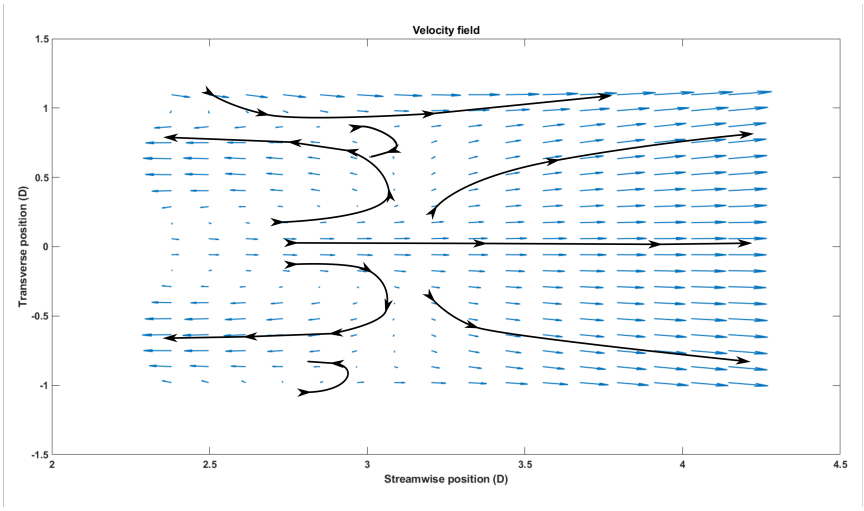

Figure 5.2: Velocity field from PIV measurements with black arrows illustrating streamlines.

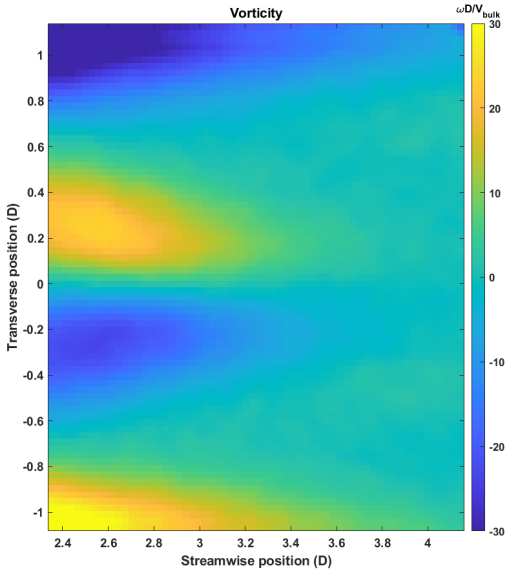

Figure 5.3: Vorticity field, obtained from PIV measurements.

The field of view from the PIV measurements covers roughly 2.4D to 4.5D in the streamwise direction and -1.1D to 1.1D in the transverse direction. This is a small area, and it does not cover the entire wake width. The FOV covers the transition from the near recirculation zone to the regular wake described in subsection 2.1.3. Here, it is expected to develop periodic shedding. Because of turbulence and 3-D effects, there might not be a typical Von Karman shedding with concentrated vorticity. In section 3.5, it is discussed that shapes with aspect ratios subceeding 7 will lose its strong and periodic shedding. Still, some sort of shedding with a certain frequency is expected. Shedding is difficult to visualize in time averaged velocity and vorticity fields because it is periodic and travels downstream. Therefore, instantaneous vorticity fields can be observed. There was not observed any vortex shedding of these fields. One example can be seen in Figure 5.4, which shows turbulent flow without any clear vortex roll up travelling downstream. A power spectrum analysis was performed in DaVis 8.4, and there was no clear sign of frequencies that dominated in the FOV either, as seen in Figure 5.5. If there was a specific dominating frequency, a big spike at this frequency, together with its harmonic frequencies, would be observed. In this plot, there are some spikes, but they do not visualize one frequency with its harmonies. There is some development in the area around 17–25Hz, which lies in the expected area using the Strouhal number for 2-D flow from Equation 2.7 and Figure 3.5, i.e. roughly 18Hz. The spikes are still too unclear to conclude if this is actually correct.

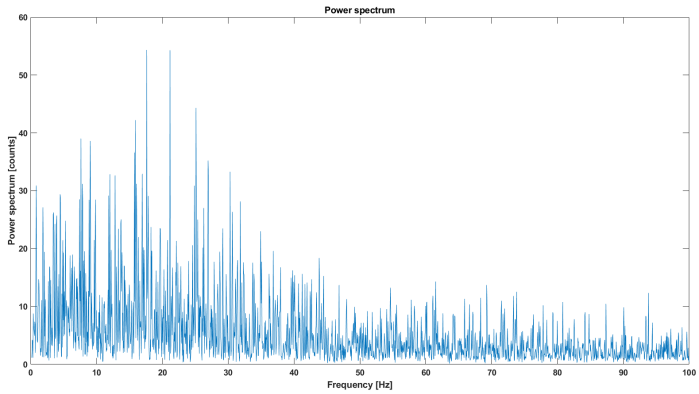

Figure 5.5: Power spectrum taken from the center line, 4D downstream. The three highest spikes are situated at the frequencies of 17.6Hz, 21.2Hz and 25.1Hz.

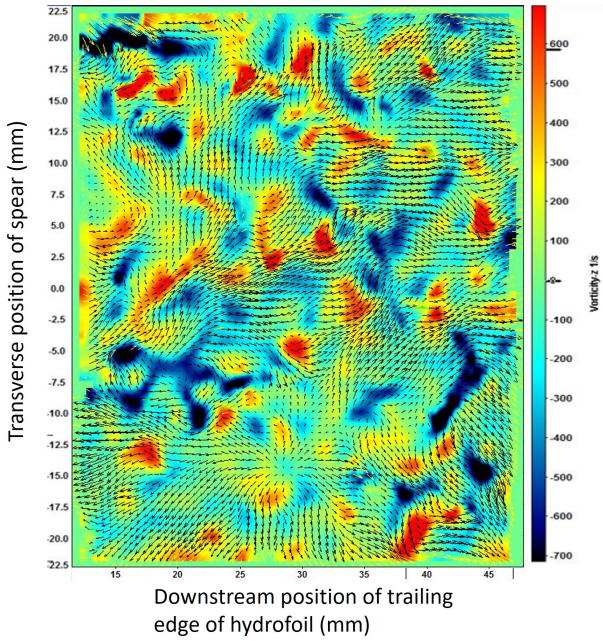

Figure 5.4: A snapshot from DaVis 8.4 of an instantaneous vorticity in the field of view.

5.2 Comparison to CFD

Figure 5.6 shows a comparison between the streamwise velocity in the FOV for the CFD and the PIV measurements, both taken from 62% of the height of the spear. To avoid big contrasts due to big differences in color extremes, the colorbar is differently scaled for each of them. Both results depict the backflow, separated by the downstream velocity, which deviates from literature in the idealized two-dimensional case. The CFD results show why this may be the case; there is a substantial downwards flow towards the ground in this plane where the downstream flow separating the backflow is present, see Figure 5.7. This is likely due to the downwash discussed in the last section, and the simulations confirm to some degree that this is the case.

In the PIV measurements, the velocity profile flattens drastically from 2.5D to 4D. This drastic change is not evident in the CFD results, as seen in Figure 5.10. The profiles start with a similar shape, but then the PIV measurement profiles flatten downstream. Comparing Figure 5.2 and Figure 5.9,

the velocity field from CFD is more complex. The circulating patterns are more scattered, and the backflow is substantially bigger above the center line than below. The PIV measurements show a more symmetrical and ordered time-averaged flow structure. They both experience the transition from back flow to downstream flow between 3D and 4D. The streamwise velocity for the full data set from the CFD results can be seen in Figure 5.8, and here it can be observed that there are clearly two regions forming at 2D downstream, and these two regions are evident to some degree to the end of the data set at 10D downstream as well.

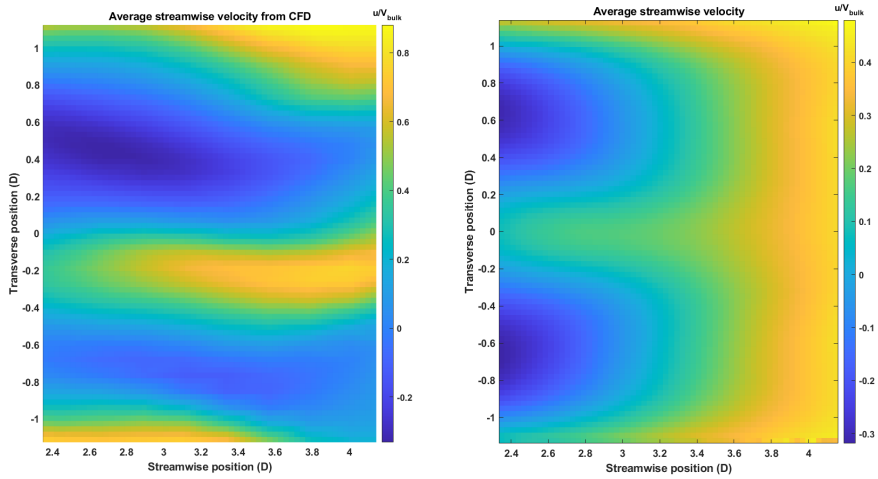

(a) **(b)**

Figure 5.6: Streamwise velocity from a) CFD simulations by Marcell Szabo-Meszaros, and b) from PIV measurements

There might be a drastic 3-D flow effect that flattens the velocity profile from the PIV measurements in the downstream part of the FOV. There might be flow that is flowing from the top of the spear, over the recirculation zone and into the wake at roughly 62% height. In that case, if the vertical placement of the measurement plane of the CFD and PIV deviate slightly, it might cause a considerable effect to the result. Looking at the vertical velocity from the CFD results in Figure 5.7, there is some indication pointing towards that the downwash is significant in the FOV, and is yet to flatten in the streamwise direction. Therefore, it would be interesting to see if there exist a significant velocity profile flattening like in the PIV measurements if

data from several planes was extracted from the CFD simulation. This data was not available when writing this discussion.

The big difference could also mean that some parts of the results are not sufficient in either PIV, CFD or both of them. The scope of this thesis does not cover a technical validation of CFD. The uncertainty of the PIV measurements will be discussed in the next section. Uncertainty in the PIV measurements aside, there could be other aspects that cause the deviation, i.e. systematic error. This is discussed in subsection 4.2.3. This shows the importance of the measurements in the new PIV rig at the big water channel that will be held shortly after this thesis is written. This rig will make it possible to expand the FOV, test the repeatability of this experiment and add more distance between the appendices and the channel walls.

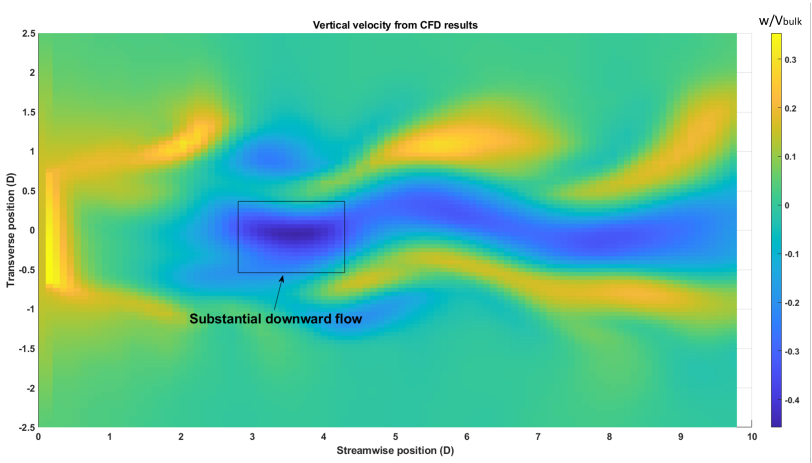

Figure 5.7: Vertical velocity from CFD results. Simulations by Marcell Szabo-Meszaros.

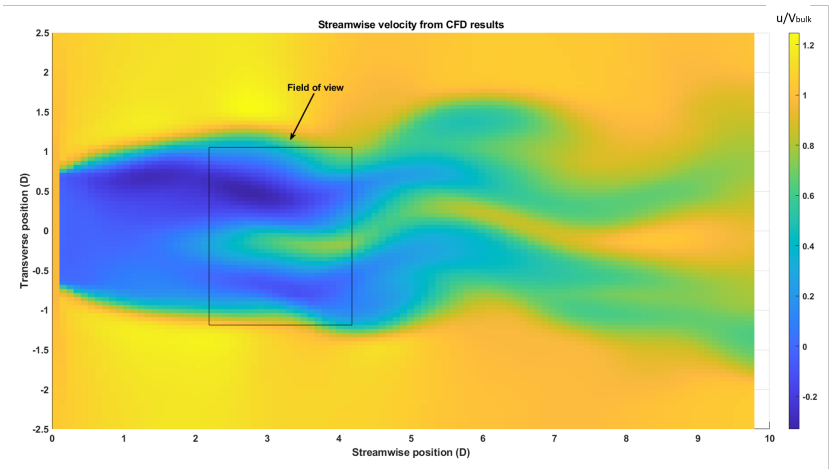

Figure 5.8: Streamwise velocity field from CFD results, from 0 to 10 diameters downstream. Simulations by Marcell Szabo-Meszaros.

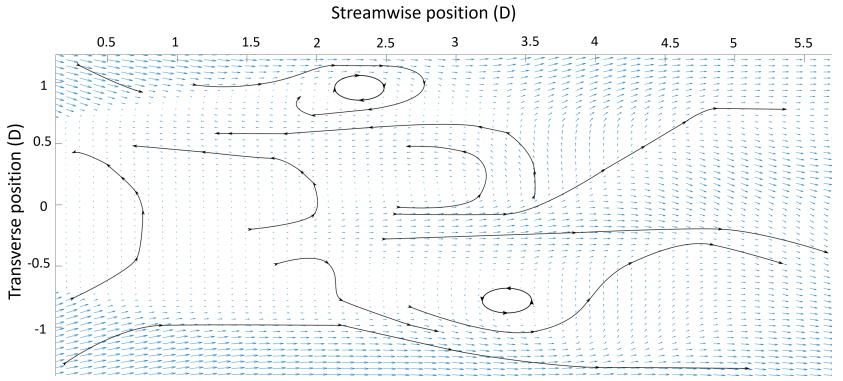

Figure 5.9: Velocity field from CFD results. The black arrows are indicating streamlines. Simulations by Marcell Szabo-Meszaros.

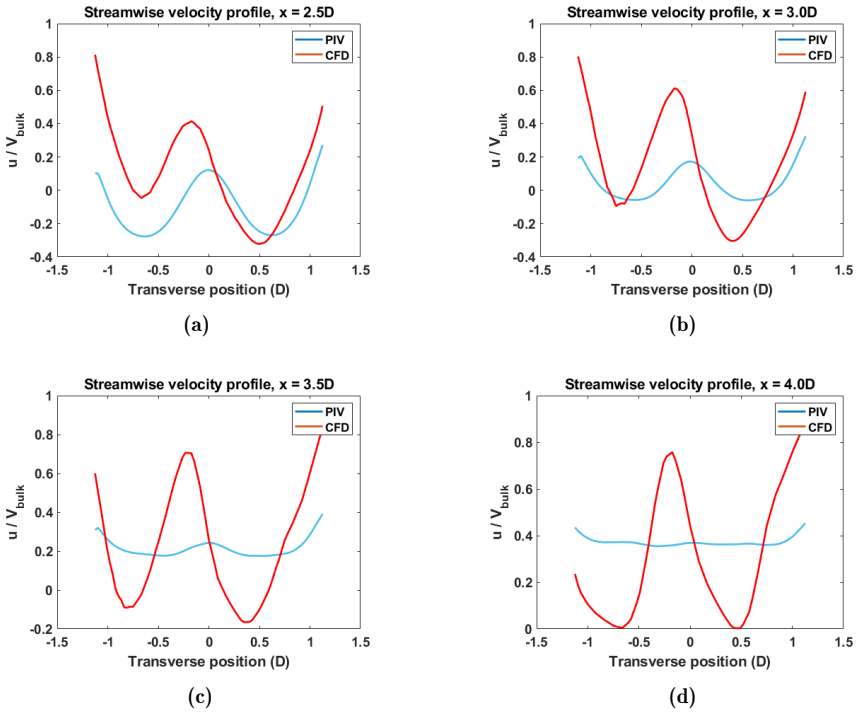

Figure 5.10: Streamwise velocity profiles from PIV measurements and CFD simulations. Simulations by Marcell Szabo-Meszaros.

5.3 Random error

DaVis 8.4 calculates the random error by Equation 2.15. Several image frequencies were tested, and the lowest possible frequency that the system allowed (200Hz) gave the smallest uncertainty. A comparison of a velocity magnitude profile of 200Hz and 800Hz can be seen in Appendix C. The empirical standard deviation for the four measurement sets using Equation 2.14 was calculated and is plotted in Figure 5.11. This shows that the standard deviation is less than 3.5% of the mean velocity magnitude in most of the FOV, except for some areas in the recirculation zone, where it is found to be roughly 5%. The empirical standard deviation of the velocity profiles at 2.5D, 3D and 4D downstream is shown in Figure 5.12. The results from Davis 8.4, as well as the empirical standard deviation calculations for the

four measurement set are deemed acceptable for the discussion done in the previous section.

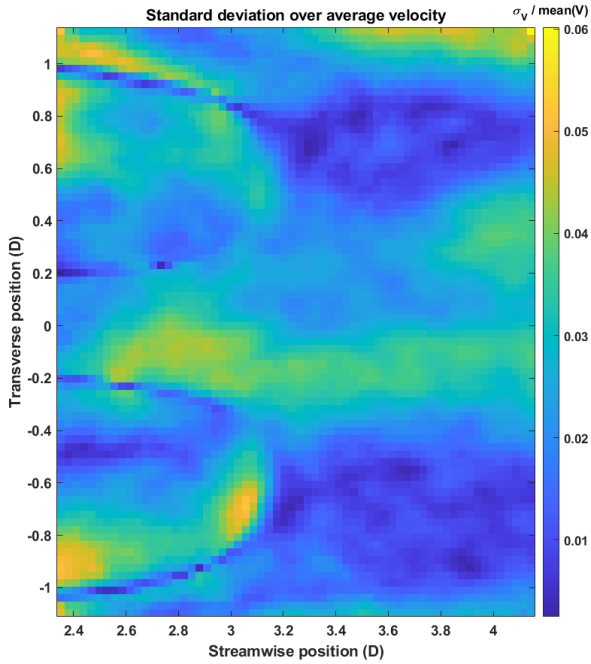

Figure 5.11: Standard deviation of the velocity magnitude from the four measurement sets.

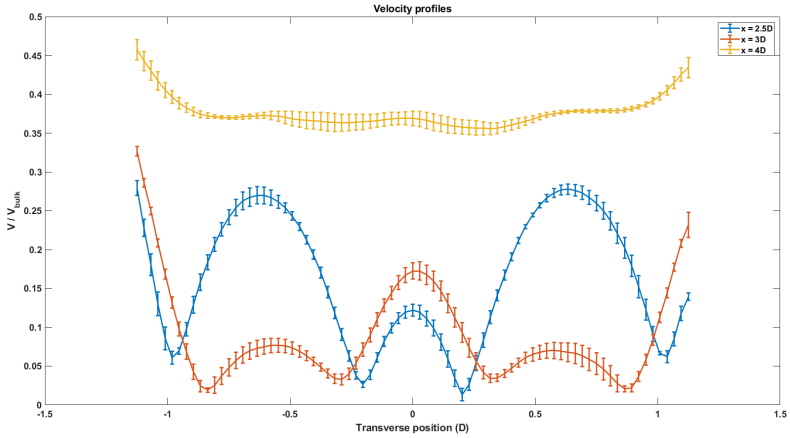

Figure 5.12: Streamwise velocity profiles with error bars calculated by the standard deviation of the four measurement sets.

5.4 Literature review

The literature review is affected by the fact that the wake behind objects is largely dependent on the Reynolds number and the exact shape of the object. Both the SINTEF simulations and literature indicate that a triangle cylinder creates a wake with more circulation than a D-cylinder. The near wake is wider and longer for the spear than the D-cylinder in the CFD simulations, and there is literature describing the low velocity zone as being smaller than for the triangle. Note that the CFD simulations described in section 3.5 have acquired data at 50% of the height of the spear, and can therefore not be compared directly to the CFD and PIV results presented previously in this chapter, which are taken from 62% of the height.

What the spear and the D-cylinder in the FishPath project will be largely dependent on is 3-D effects. They have an aspect ratio between 1 and 2, which indicates highly three-dimensional flow. The literature reviewed states that for these aspect ratios, periodic shedding is lost, there is a significant downwash force and the vortices formed in the recirculation zone will be elongated and more symmetrical. The turbulence intensity component in the vertical direction will be greater than in the streamwise and transverse directions. It is not clear how these 3-D effects differ from the spear and D-cylinder. This would be interesting to find in future experiments because

the 3-D effects are dominating over the 2-D effects in the appendices studied for FishPath.

The delta ramp has not been extensively studied in subsonic flows, but what is known is that they create streamwise vortices. The delta ramp was chosen as opposed to the delta wing, which is the same shape but turned backwards, because it does not catch particles in a river. However, for the FishPath project, a version was chosen where the delta ramp was filled underneath with material from top to ground level, see Figure 3.12. This would have made the delta wing less prone to catching particles. From literature, there is indications that the delta ramp creates streamwise vortices that will be stronger and last longer, which is better for the project. This has not yet been tested for a filled version of the wing, but it should be considered. The delta wing vortices are not in the scope of this thesis and are more thoroughly discussed in the project thesis of the author [1].

Chapter 6

Conclusions

The purpose of this master thesis was to contribute to the FishPath project, which seeks to find relations between hydrodynamic properties in a river and how these affect migrating fish. A literature review on the hydrodynamic properties of wakes behind three types of appendices that will be mounted on a hydrofoil in the project was conducted. SINTEF has provided computational fluid dynamics (CFD) simulations for these three appendices, which are cylinders with triangular and D-shaped cross sections, denoted spear and D-cylinder respectively, and the delta ramp vortex generator. Particle image velocimetry (PIV) was conducted on similar setup with the spear in a test rig at the Waterpower Laboratory (VKL) with the purpose of investigating if the CFD and PIV measurements exhibit roughly the same flow properties.

The literature indicates that the spear and D-cylinder can create vertical and horizontal vortices, where the spear creates a wake that is wider and has stronger circulation. Stronger circulation can be achieved with larger appendices. Both of the cylindrical geometries have an aspect ratio of between one and two, and the literature states that resulting flow fields will be largely affected by three dimensional flow. Strong periodic shedding will not be as evident, the vortex formation region in the near wake will be elongated and symmetric, and the vertical and horizontal vortices expected are not as governing as in an idealized two-dimensional flow. For these types of aspect ratios, there is likely a bigger turbulent intensity component in the vertical direction than in the components created by the two dimensional flow components. The delta ramp vortex generator is expected to create a pair of streamwise vortices, but will likely lose its vorticity quickly. A delta wing vortex generator will most likely create stronger vortices and last longer. There has been a concern that a delta wing will catch particles in a river, but because the objects will be filled underneath to be able to attach them

to a hydrofoil more easily, this will not be an issue.

The PIV measurements of the spear show the transition between the recirculation zone and the regular wake, and cover 2.4D to 4.5D downstream and -1.1D to 1.1D transversely. Two clearly visible regions of circulating backflow separated by downstream flow are visible in the upstream part of the Field of View (FOV). This type of flow deviates from the typical recirculating area in two dimensional flow, and is likely due to large three dimensional effects. At roughly 3.5D, there is a sudden transition where the backflow disappears and the velocity profiles flatten. The CFD simulations also predict the two circulating backflow regions separated by downstream flow. The velocity profiles at this point coincide well with the measurements, but are less symmetrical. However, the transition between the recirculating zone is not as drastic in the simulations. At 4.5D the results start to deviate significantly. The cause of this might be a deviation in the vertical height of the measurement planes, because this placement is very sensitive to which 3-D effects that are evident. It could also be a systematic error from the PIV (the random error is deemed acceptable) or something that is insufficient about the CFD simulations. A technical CFD validation and a new PIV measurement with a larger FOV and a more similar experimental set-up to the CFD simulation should be considered.

This master thesis has described important flow properties of the wakes behind structures that will be used in the FishPath project, shown similarities between experiments and CFD simulations, and includes the first PIV measurements at VKL in two years, which will serve as a starting point for many more measurements to come. Work on the design of the PIV setup at another facility at VKL has also been done. If the PIV experiments at VKL and the CFD simulations from SINTEF can together describe the hydrodynamic properties of several appendices, FishPath can relate these properties to how fish react to them in experiments. If the knowledge on these relations is uncovered, a low-cost and reliable method to guide fish away from hydropower intakes can be made, thus reducing the fish mortality today drastically.

Chapter 7

Future work

Data from the CFD simulations should be extracted from several planes near 62% of the height of the spear to see if there exist a drastic velocity profile flattening like in the PIV measurements. This thesis is part of the beginning of the FishPath project and one PIV campaign was completed on a single appendix with a small field of view. More measurements in the water channel at the Waterpower Laboratory should be done on all three types of appendices with a larger field of view. Preferably, measurements over several planes and with a domain that is more geometrically similar to the simulations. This, together with a CFD validation on why there was deviation in the wake at four diameters downstream, should be done to be able to progress further in the project. Next, more CFD simulations and experiments on the wake of several appendices next to each other should be performed. When hydraulic descriptions of the wakes behind several appendices are achieved, these descriptions can be compared to how the fish reacts, thus increasing the knowledge of influencing fish migration.

References

[1] Urdahl, S., 2021, "Influencing fish migration by creating and altering vortices in turbulent flow," M.Sc. thesis/project, Institutt for energi-og prosessteknikk, NTNU.

[2] Griffin, O. M. and Ramberg, S. E., 1974, "The vortex-street wakes of vibrating cylinders," Journal of Fluid Mechanics, **66**(3), p. 553–576.

[3] Raffel, M., Willert, C. E., Scarano, F., Kähler, C. J., Wereley, S. T., and Kompenhans, J., *Particle Image Velocimetry: A Practical Guide*, 3rd ed., Springer International Publishing, Cham.

[4] Shanbhogue, S. J., Husain, S., and Lieuwen, T., 2009, "Lean blowoff of bluff body stabilized flames: Scaling and dynamics," Progress in energy and combustion science, **35**(1), pp. 98–120.

[5] Guo, C., Guo, H., Hu, J., Song, K., Zhang, W., and Wang, W., 2019, "Large Eddy Simulation of Flow over Wavy Cylinders with Different Twisted Angles at a Subcritical Reynolds Number," Journal of Marine Science and Engineering, **7**(7).

[6] Blevins, R. D., 1994, "Flow-induced vibration," .

[7] Mohd Kazim, M. N. F., Rasani, R., Nuawi, M. Z., Harun, Z., Khang Hau, Y., and Abdul Majid, M. S., 2020, "Analysis of Wake Region Behind Bluff Body for Piezoelectric Energy Harvester," Journal of Advanced Research in Fluid Mechanics and Thermal Sciences, **55**(2), p. 249–263.

[8] WANG, H. F. and ZHOU, Y., 2009, "The finite-length square cylinder near wake," Journal of fluid mechanics, **638**, pp. 453–490.

[9] WANG, H. F. and ZHOU, Y., 2009, "The finite-length square cylinder near wake," Journal of fluid mechanics, **638**, pp. 453–490.

[10] Rajasekaran, J., 2022, "On the flow characteristics behind a backward-facing step and the design of a new axisymmetric model for their study," .

[11] Shigeru Ogawa, S. U., 2018, "Heat Transfer Enhancement by Vortex Generators for Compact Heat Exchanger of Automobiles," , pp. 321–330.

[12] P.R. Shukla, R. S. A. A. K. R. v. D. D. M. M. P. S. S. P. V. R. F. M. B. A. H. G. L. S. L. J. M. e., J. Skea, 2022, "Climate Change 2022: Mitigation of Climate Change. Contribution of Working Group III to the Sixth Assessment Report of the Intergovernmental Panel on Climate Change," Cambridge University Press, Cambridge.

[13] Bartle, A., 2002, "Hydropower potential and development activities," Energy policy, **30**(14), pp. 1231–1239.

[14] Mussa, M., Teka, H., and Ayicho, H., 2018, "Environmental Impacts of Hydropower and Alternative Mitigation Measures," .

[15] Çengel, Y. A., 2014, "Fluid mechanics : fundamentals and applications," .

[16] Anderson, J. D., 2017, *Fundamentals of aerodynamics*, sixth edition, international student edition. ed., McGraw-Hill, New York.

[17] Pope, S. B., 2000, "Turbulent flows," .

[18] Westerweel, J., 1993, "Digital particle image velocimetry : theory and application," .

[19] *GmbH 2017 Lavision software davis 8.4 product-manual, item-number: 1105xxx document name: 1003001 DaVis D84.pdf.*

[20] Cote, A. J. and Webb, P. W., 2015, "Living in a turbulent world - A new conceptual framework for the interactions of fish and eddies," *Integrative and Comparative Biology*, Vol. 55, Oxford University Press, Paper No. 4.

[21] Derakhshandeh, J. and Alam, M. M., 2019, "A review of bluff body wakes," Ocean engineering, **182**, pp. 475–488.

[22] Forouzi Feshalami, B., He, S., Scarano, F., Gan, L., and Morton, C., 2022, "A review of experiments on stationary bluff body wakes," Physics of Fluids, **34**(1).

[23] Uffinger, T., Ali, I., and Becker, S., 2013, "Experimental and numerical investigations of the flow around three different wall-mounted cylinder geometries of finite length," Journal of wind engineering and industrial aerodynamics, **119**, pp. 13–27.

[24] Sumner, D., Heseltine, J. L., and Dansereau, O. J. P., 2004, "Wake structure of a finite circular cylinder of small aspect ratio," Experiments in fluids, **37**(5), pp. 720–730.

[25] Park, C.-W. and Lee, S.-J., 2000, "Free end effects on the near wake flow structure behind a finite circular cylinder," Journal of wind engineering and industrial aerodynamics, **88**(2), pp. 231–246.

[26] Budair, M., Ayoub, A., and Karamcheti, K., 1991, "Frequency measurements in a finite cylinder wake at a subcritical Reynolds number," AIAA journal, **29**(12), pp. 2163–2168.

[27] Sakamoto, H. and Arie, M., 1983, "Vortex shedding from a rectangular prism and a circular cylinder placed vertically in a turbulent boundary layer," Journal of fluid mechanics, **126**, pp. 147–165.

[28] Okamoto, S. and Sunabashiri, Y., 1992, "Vortex Shedding From a Circular Cylinder of Finite Length Placed on a Ground Plane," Journal of fluids engineering, **114**(4), pp. 512–521.

[29] Galbraith, M., Orkwis, P., and Benek, J., 2009, "Multi-Row Micro-Ramp Actuators for Shock Wave Boundary-Layer Interaction Control," pp. 1–30, doi:10.2514/6.2009-321.

[30] Zhang, H., 2017, "The Water Tunnel/Channel Design and Application in Beihang University," .

[31] Roque, G., Ássi, S., Meneghini, J. R., Augusto, J., Aranha, P., George, W., and Coleto, P., 2005, "Design, assembling and verification of a circulating water channel facility for fluid dynamics experiments," .

[32] Eslam Panah, A. and Barakati, A., 2017, "Design and Build a Water Channel for a Fluid Dynamics Lab," .

[33] Mehta, R. and Bradshaw, P., 1979, "Design rules for small low speed wind tunnels," Aeronautical journal, **83**(827), pp. 443–453.

[34] Johl, G., Passmore, M., and Render, P., 2004, "Design methodology and performance of an indraft wind tunnel," Aeronautical journal, **108**(1087), pp. 465–473.

[35] Mauro S., L. R. F. F. G. A., Brusca S.b and M, M., 2017, "Small-Scale Open-Circuit Wind Tunnel: Design Criteria, Construction and Calibration," International Journal of Applied Engineering, **12**(23), pp. 13649–13662.

Appendices

Master thesis agreement

Norwegian University of Science and Technology

Faculty of Engineering
Department of Energy and Process Engineering

NTNU

MASTER THESIS
for
student Simon Margido Urdahl

Spring 2022

FishPath

Background

Safe passage of downstream migrating fish is a challenge for the hydropower industry. The number of fish entering the intake to existing hydropower plants is often too high and fish mortality should be reduced. Currently available solutions depend on retrofitting of large fined meshed rack- and bypass constructions. In this project, alternative solutions are investigated based on behavioral guiding of fish. Research on alternative behavioral guiding systems is currently rather limited, focusing on guiding racks or repulsion systems. However, recent advances in the knowledge on behavioral responses to turbulence eddies point toward the possibility of exploiting the species innate attraction and repulsion for eddies of different characteristics to create migration paths passed the intakes. It has been shown that some eddies may boost swimming whereas others can hamper swimming. Turbulence eddies may be crated in new rack designs or alternative structures that efficiently interconnects the desired turbulence eddies into a migration path. Such constructions are expected to be less demanding both technologically and in terms of cost.
The FishPath-project is a project funded by the Norwegian Research Council and the student will be a part of the project team.

Objective

To explore the possibility of using inter-connected turbulence eddies as paths for fish downstream migration passed hydropower intakes

The following tasks are to be considered:

1. Literature study
    a. Turbulent eddies/ vortices
    b. Vortex generators
2. Software knowledge
    a. MATLAB or Python will be used for the evaluation of the measurements
3. Preparations in the Waterpower Laboratory
    a. Learn how to use the PIV-measurement system
    b. Installation of a vortex generators
4. Measurements in the Waterpower Laboratory:
    a. Calibration of the PIV
    b. Velocity measurements by utilizing PIV-measurements

Address
N-7034 Trondheim
Norway

Location
K. Hejes vei 1b

Tel. +47 73 59 38 60
Fax +47 73 59 35 80
Org. no. NO 974 767 880

The work shall be edited as a scientific report, including a table of contents, a summary in English, conclusion, an index of literature etc. When writing the report, the candidate must emphasise a clearly arranged and well-written text. To facilitate the reading of the report, it is important that references for corresponding text, tables and figures are clearly stated both places.
By the evaluation of the work the following will be greatly emphasised: The results should be thoroughly treated, presented in clearly arranged tables and/or graphics and discussed in detail.

The candidate is responsible for keeping contact with the subject teacher and teaching supervisors.

Risk assessment of the candidate's work shall be carried out according to the department's procedures. The risk assessment must be documented and included as part of the final report. Events related to the candidate's work adversely affecting the health, safety or security, must be documented and included as part of the final report. If the documentation on risk assessment represents a large number of pages, the full version is to be submitted electronically to the supervisor and an excerpt is included in the report.

According to “Utfyllende regler til studieforskriften for teknologistudiet/sivilingeniørstudiet ved NTNU” § 20, the Department of Energy and Process Engineering reserves all rights to use the results and data for lectures, research and future publications.

Submission deadline: 13th June 2022.

☒ Work to be done in the Waterpower Laboratory
☐ Field work

Department for Energy and Process Engineering, *10th January 2022*

_____
Ole Gunnar Dahlhaug
Supervisor

Co-Supervisors: Bjørn Winther Solemslie (Bjorn.Solemslie@nina.no)
Kristian Sagmo (Kristian.Sagmo@ntnu.no)

Appendices

Porosity of the honeycomb cell structure

Each honeycomb cell have a structure that is associated with it. From Figure B.1 one can see that the structure can be divided into six rectangles (blue) and six shapes connecting them (red). The shapes is one third of an equilateral triangle with sides equal to the wall thickness (w). The rectangles have a length equal to the side length of the cells (s) and a width of half the structure thickness (w/2). The area ($A_{hexagon}$) and cell size (d_{cell}) are given in Equation B.1 and Equation B.2 respectively.

$$A_{hexagon} = \frac{3\sqrt{3}s^2}{2} \tag{B.1}$$

$$d_{cell} = \sqrt{2}s \tag{B.2}$$

This concludes that the structure to flow ratio (r) is given by

$$r = \frac{2}{\sqrt{3}}\frac{w}{s} + \frac{1}{3}(\frac{w}{s})^2 \tag{B.3}$$

By knowing the flow ratio, the porosity of the structure (β, i.e area of flow to area of test section ratio) can be found, using Equation B.4. This equation is not true for the sides of the the honeycomb plate depending on where it is cut. In this analysis, the effect of the sides are negligible due to the amount of cells in the honeycomb plate.

$$\beta = \frac{1}{1+r} \tag{B.4}$$

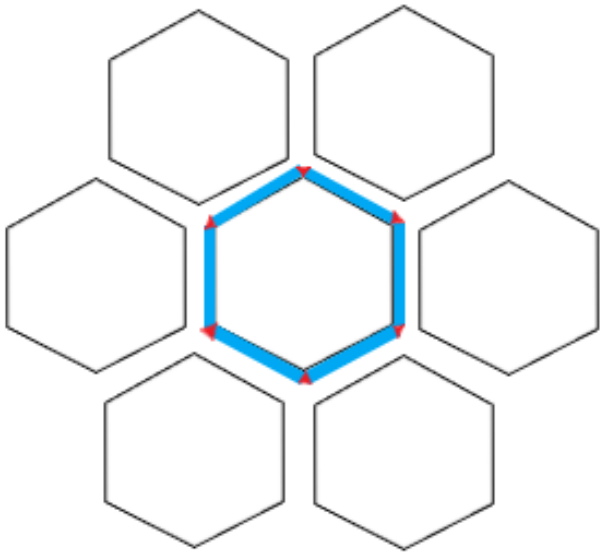

Figure B.1: Structure around a honeycomb cell in a flow straightener. Blue shapes are rectangles and red shapes are one third of equilateral triangles.

Appendices

Uncertainty for different image acquisition rates

Figure C.1 shows that the error bars, and therefore the uncertainty, are significantly greater at 800Hz than for 200Hz. This is why 200Hz image acquisition rate have been chosen.

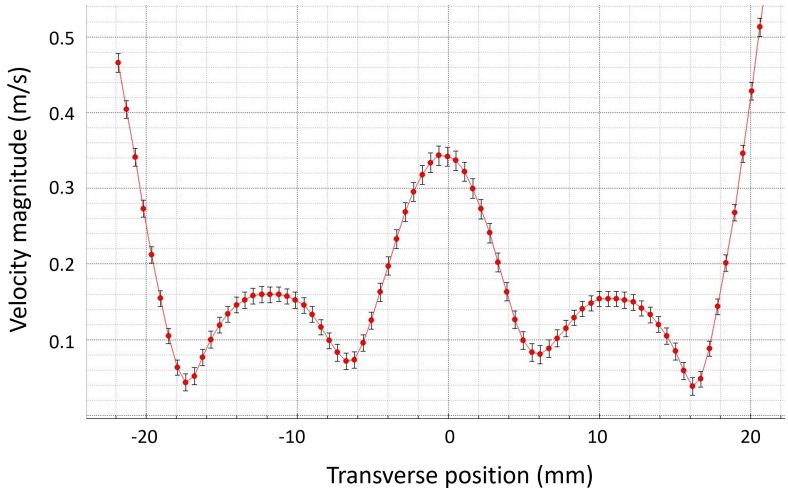

(a)

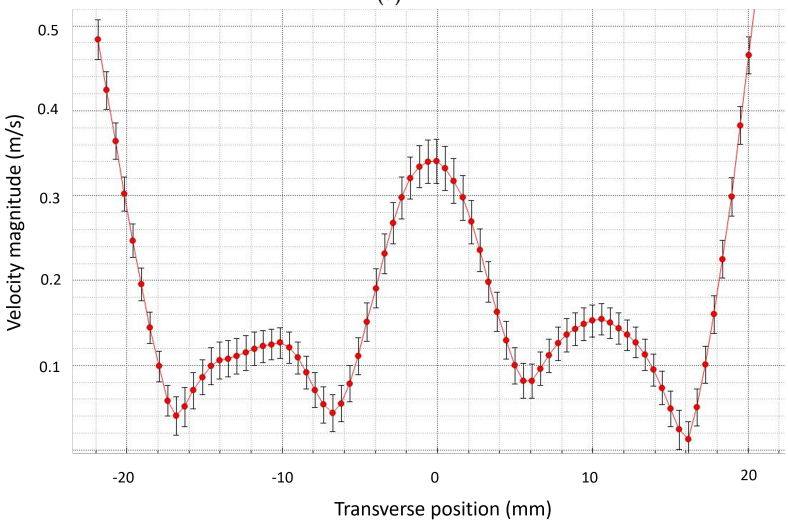

(b)

Figure C.1: Velocity magnitude profiles at x = 3D downstream with an image acquisition rate of a) 200Hz, b) 800Hz

Appendices

HSE form

NTNU HMS	Kartlegging av risikofylt aktivitet	Utarbeidet av	Nummer	Dato
		HMS-avd.	HMSRV2601	22.03.2011
		Godkjent av	Side	Erstatter
		Rektor		01.12.2006

Enhet: Vannkraftlaboratoriet **Dato:** 13.05.2022

Linjeleder: Ole Gunnar Dahlhaug

Deltakere ved kartleggingen (m/ funksjon):
(Ansv. veileder, student, evt. medveiledere, evt. andre m. kompetanse) *Simon Urdahl (student), Ole Gunnar Dahlhaug (veileder)*

Kort beskrivelse av hovedaktivitet/hovedprosess: Masteroppgave - Simon Urdahl. Influencing fish migration by creating and altering vortices in turbulent flow

Er oppgaven er rent teoretisk? *(JA/NEI)* Nei *"JA" betyr at veileder innestår for at oppgaven ikke innholder noen aktiviteter som krever risikovurdering*

Dersom "JA": Beskriv kort aktiviteten i kartleggingskjemaet under. Risikovurdering trenger ikke å fylles ut.

Signaturer: *Ansvarlig veileder:* Ole G. Dahlhaug *Student:* Simon Urdahl

ID nr.	Aktivitet/prosess	Ansvarlig	Eksisterende dokumentasjon	Eksisterende sikringstiltak	Lov, forskrift o.l.	Kommentar
1	Particle Image Velocimetry - Eksperiment med bruk av laser	Kristian Sagmo	Risk Assesment Report	Opplæring, Risikovurdering		
2						
3						
4						
5						
6						

NTNU / HMS /KS	Risikovurdering	Utarbeidet av	Nummer	Dato
		HMS-avd.	HMSRV2603	04.02.2011
		Godkjent av	Side	Erstatter
		Rektor		09.02.2010

Enhet: Vannkraftlaboratoriet **Dato:** 13.05.2022

Linjeleder: Ole Gunnar Dahlhaug

Deltakere ved risikovurderingen (m/ funksjon):
(Ansv. veileder, student, evt. medveiledere, evt. andre m. kompetanse) *Simon Urdahl (student), Ole Gunnar Dahlhaug (veileder)*

Risikovurderingen gjelder hovedaktivitet: Masteroppgave - Simon Urdahl. Influencing fish migration by creating and altering vortices in turbulent flow

Signaturer: *Ansvarlig veileder:* Ole G. Dahlhaug *Student:* Simon Urdahl

ID nr.	Aktivitet/prosess fra kartleggingsskjemaet	Mulig uønsket hendelse	Vurdering av sannsynlighet (1-5)	Vurdering av konsekvens				Risikoverdi (menneske)	Kommentarer/ status Forslag til tiltak
				Menneske (A-E)	Ytre miljø (A-E)	Øk./ materiell (A-E)	Omdømme (A-E)		
1	Particle Image Velocimetry - Eksperiment med bruk av laser	Skade på øyne ved feil bruk av laser	1	D	A	A	D	D1	Bygges et telt rundt eksperimentet, og når laser brukes vil man ikke være i teltet. Vil få opplæring og prosedyrer av teknisk personell.
1	Particle Image Velocimetry - Eksperiment med bruk av laser	Uønsket refleksjon av laserstråle.	1	B	A	A	A	B1	Bygges et tykt telt rundt eksperimentområdet.
1	Particle Image Velocimetry - Eksperiment med bruk av laser	Folk går inn i teltet uten beskyttelsesbriller.	2	C	A	A	A	C2	Tydelig merking av området, med skilt.
1	Particle Image Velocimetry - Eksperiment med bruk av laser	Ødelegge labutstyr	2	A	A	B	B	A2	Akseptabel risiko.
1	Particle Image Velocimetry - Eksperiment med bruk av laser	Vannskade på labutstyr	3	A	A	B	B	A3	Akseptabel risiko.

1	Particle Image Velocimetry - Eksperiment med bruk av laser	Strukturell feil pga høyt trykk	1	A	C	C	C	A1	Akseptabel risiko.

Risikoverdi = Sannsynlighet (1, 2 ...) x konsekvens (A, B ...). Risikoverdi A1 betyr svært liten risiko. Risikoverdi E5 betyr svært stor og svært alvorlig risiko.

Sannsynlighet		Konsekvens					
Verdi	Kriterier	Gradering		Menneske	Ytre miljø: Vann, jord og luft	Øk/materiell	Omdømme
1	**Svært liten**:1 gang pr 50 år eller sjeldnere	E	Svært alvorlig	Død	Svært langvarig og ikke reversibel skade	Drifts- eller aktivitetsstans >1 år.	Troverdighet og respekt betydelig og varig svekket
2	**Liten**: 1 gang pr 10 år eller sjeldnere	D	Alvorlig	Alvorlig personskade. Mulig uførhet	Langvarig skade. Lang restitusjonstid	Driftsstans > ½ år, aktivitetsstans opptil 1 år	Troverdighet og respekt betydelig svekket
3	**Middels**: 1 gang pr år eller sjeldnere	C	Moderat	Alvorlig personskade.	Mindre skade og lang restitusjonstid	Drifts- eller aktivitetsstans < 1 mnd	Troverdighet og respekt svekket
4	**Stor**: 1 gang pr måned eller sjeldnere	B	Liten	Skade som krever medisinsk behandling	Mindre skade og kort restitusjonstid	Drifts- eller aktivitetsstans < 1uke	Negativ påvirkning på troverdighet og respekt
5	**Svært stor** :Skjer ukentlig	A	Svært liten	Skade som krever førstehjelp	Ubetydelig skade og kort restitusjonstid	Drifts- eller aktivitetsstans < 1dag	Liten påvirkning på troverdighet og respekt

MATRISE FOR RISIKOVURDERINGER ved NTNU

KONSEKVENS						
	Svært alvorlig	E1	E2	E3	E4	E5
	Alvorlig	D1	D2	D3	D4	D5
	Moderat	C1	C2	C3	C4	C5
	Liten	B1	B2	B3	B4	B5

	Svært liten	A1	A2	A3	A4	A5
		Svært liten	Liten	Middels	Stor	Svært stor
		SANNSYNLIGHET				

Prinsipp over akseptkriterium. Forklaring av fargene som er brukt i risikomatrisen.

Farge	Beskrivelse
Rød	Uakseptabel risiko. Tiltak skal gjennomføres for å redusere risikoen.
Gul	Vurderingsområde. Tiltak skal vurderes.
Grønn	Akseptabel risiko. Tiltak kan vurderes ut fra andre hensyn.

Simon Margido Urdahl

Influencing fish migration by creating and altering vortices in turbulent flow

NTNU
Norwegian University of
Science and Technology